ABSTRACT

Title of Document: INVESTIGATION OF LOW TEMPERATURE SOLID OXIDE FUEL CELLS FOR AIR-INDEPENDENT UUV APPLICATIONS

Jennie Mariko Moton, Master of Science, 2012

Directed By: Professor Gregory S. Jackson, Department of Mechanical Engineering

Unmanned underwater vehicles (UUVs) will benefit greatly from high-energy-density (> 500 Wh/L) power systems utilizing high-energy-density fuels and air-independent oxidizers. Current battery-based systems have limited energy densities (< 200 Wh/L), which motivate development of alternative power systems such as solid oxide fuel cells (SOFCs). SOFC-based power systems have the potential to achieve the required UUV energy densities, and the current study explores how SOFCs based on gadolinia-doped ceria (GDC) electrolytes with operating temperatures of 650°C and lower may operate in the unique environments of a promising UUV power plant. The plant would contain a H_2O_2 decomposition reactor to supply humidified O_2 to the SOFC cathode and exothermic aluminum/H_2O combustor to provide heated humidified H_2 fuel to the anode.

To characterize low-temperature SOFC performance with these unique O_2 and H_2 source, SOFC button cells based on nickel/GDC ($Gd_{0.1}Ce_{0.9}O_{1.95}$) anodes, GDC electrolytes, and lanthanum strontium cobalt ferrite ($La_{0.6}Sr_{0.4}Co_{0.2}Fe_{0.8}O_{3-\delta}$ or LSCF)/GDC cathodes were fabricated and tested for performance and stability with humidity on both the anode and the cathode. Cells were also tested with various reactant concentrations of H_2 and O_2 to simulate gas depletion down the channel of an SOFC stack. Results showed that anode performance depended primarily on fuel concentration and less on the concentration of the associated increase in product H_2O. O_2 depletion with humidified cathode flows also caused significant loss in cell current density at a given voltage. With the humidified flows in either the anode or cathode, stability tests of the button cells at 650 °C showed stable voltage is maintained at low operating current (0.17 A/cm^2) at up to 50 % by mole H_2O, but at higher current densities (0.34 A/cm^2), irreversible voltage degradation occurred at rates of less than 4.0 mV/hour depending on exposure time. From these button cell results, estimated average current densities over the length of a low-temperature SOFC stack were estimated and used to size a UUV power system based on Al/H_2O oxidation for fuel and H_2O_2 decomposition for O_2. The resulting system design suggested that energy densities above 300 Wh/L may be achieved at neutral buoyancy with seawater if the cell is operated at high reactant utilizations in the SOFC stack for missions longer than 20 hours.

INVESTIGATION OF LOW TEMPERATURE SOLID OXIDE FUEL CELLS FOR AIR-INDEPENDENT UUV APPLICATIONS

By

Jennie Mariko Moton

Thesis submitted to the Faculty of the Graduate School of the

University of Maryland, College Park, in partial fulfillment

of the requirements for the degree of

Master of Science

2012

Advisory Committee:
Prof. Gregory Jackson, Chair
Prof. Eric Wachsman
Prof. Christopher Cadou

Dedication

For Fredia

Acknowledgements

To whom I owe my heartfelt gratitude, Dr. Jackson has provided me with guidance and support throughout my UMD experience, and for that I thank him for his unwavering commitment and faith in his students. I believe few have the privilege of working with an aspiring mentor and I feel honored to have been in his research group.

I thank Michelle Anderson and Maria Medeiros from the Office of Naval Research, making this research project possible through the University Lab Initiative. I also thank Dr. Joe Fonatine, Dr. Lou Carreiro, and Dr. Burke for their support and kindness at the Naval Undersea Warfare Center.

To my thesis committee, Dr. Eric Wachsman and Dr. Chris Cadou, I appreciate your time in reviewing my thesis.

For all the time taken to talk with me about SOFC button cell fabrication, I thank Colin Gore, Dr. Hee Sung Yoon, and Dr.Kang Taek Lee.

Thank you to my colleagues and lab mates for attending to my everyday questions concerns and challenges. I appreciate all their help in lab and encouragement throughout the toughest of times. Lei Wang, Daniel Ettehadieh, Will Gibbons, Tracy Liu, Andy Oles, Jon Angle, Josh Pearlman, and Rick Stroman I owe much gratitude for their support.

Last but not least, to my family with all their loving support, I owe you so much. And to Fredy who has been there for me, and always kept me motivated.

Table of Contents

List of Tables

List of Figures

Chapter 1: Introduction

1.1. Introduction to UUV Requirements

The US Navy uses unmanned underwater vehicles (UUVs) for many operations including detection, classification, and neutralization of mines, and surveillance of submarines. These types of UUV missions require a high-energy-density (energy per unit volume) and specific energy (energy per unit mass) for the vessel to sustain a long term mission without refueling. The high-energy-density requirement provides opportunities for novel energy dense propulsion systems with unique design criteria [1]. Table 1.1 lists the specifications for a Heavy Weight Vehicle (HWV) Class UUV with a torpedo-like casing for deployment from a submarine. As cost is not as stringent an issue as in many commercial applications, the principal design criteria are energy density and specific energy of the entire system, reliability, and maintaining near neutral buoyancy for underwater operations.

Table 1.1 Naval requirements for a HWV Class UUV[1]. Dimensions are given for a torpedo like hull so that UUVs may be deployed from submarines in the same way a torpedo is deployed.

Navy Requirements for UUV	
Vehicle Length (m)	1.09
Vehicle Dia (m)	0.47
Mass (kg)	209
Power (kW)	2.5 (max continuous load)
Voltage Load (V)	70-80 buss with 28V for vehicle system sensors
Energy Capacity (kWh)	100
Specific Energy (Wh/kg)	450 (minimum 300)
Energy Density (Wh/L)	500 (minimum 360)
Endurance (hours)	40

The types of missions required by the HWV Class UUV include tactical intelligence, surveillance, and reconnaissance (ISR), oceanography, mine countermeasures clandestine reconnaissance, and submarine decoy. With these types of missions there is a need for safety and stealth, in addition to the reliability, neutral buoyancy, and energy density requirements [2].

Neutral buoyancy requires that the density of the power generation system be equivalent to that of sea water, ~1,025 kg/m^3. If the system has a smaller density than sea water, or products from the power system exhaust move within the UUV, ballasting with sea water can correct the density of the system or compensate for a shift in weight to maintain a center of gravity.

Determining the energy density of a UUV propulsion system requires performing a complete balance of plant (BOP) analysis that includes any necessary fuel processing and/or oxidizer reactions, power generation device, heat exchangers, blowers/pumps, and/or electronics. These components contribute to

parasitic power losses and to total volume of the vehicle. The smaller the BOP load, the more space remains available for total fuel and oxidizer storage to allow the UUV to sustain longer missions. Of course, the energy density of the fuel/oxidizer combination also impacts mission life. Various fuel and oxidizer combinations for high-energy-density continue to be investigated for different power generation devices including fuel cells, Sterling engines, and turbines [1, 3, 4]. The energy density of the UUV power plant also depends on the thermal efficiency of the power generator in converting the fuel and oxidizer to electric and/or propulsive power.

Hydrocarbon fuels with energy densities (as high as 36 MJ of chemical energy per liter) are often preferred for military applications but they present difficult challenges for UUV propulsion systems. Hydrocarbon fuels on UUVs require an oxidizer which must be stored, and for UUVs requiring stealth operation, product CO_2 from hydrocarbon oxidation must be captured and stored. Absorption systems for CO_2 such as calcium oxide CaO can be extremely bulky and drive the effective energy density of the total system to unacceptably low levels. One study predicted this type of system to be less energy dense with a CO_2 scrubber volume of 90 liters, reducing the energy density by 197Wh/L for a 30 hour mission [5].

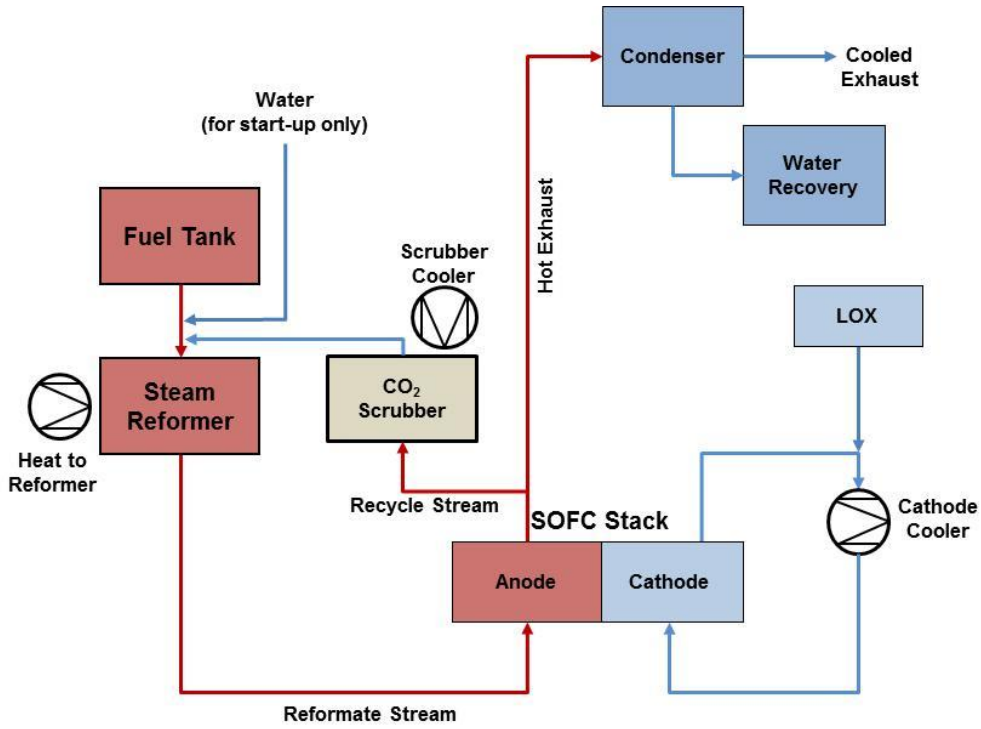

Figure 1.1 Design of a SOFC system utilizing carbonaceous fuel requiring a steam reformer and CO_2 scrubber [5].

Figure 1.1 shows the schematic for this 2.5 kW net power solid oxide fuel cell (SOFC) system with energy density of 320 Wh/L and specific energy of 325 Wh/kg for 30 hours. An ideal fuel for a UUV would only require a processing step with reusable exhaust, avoiding product absorption and allowing more space dedicated to fuel/oxidizer storage.

Currently deployed UUVs use batteries, among which the best Li-ion battery systems approach energy densities of 400 Wh/l and specific energies of 160 Wh/kg [6]. These values however, do not include neutral buoyancy considerations to equal the density of seawater. More recent research in UUV power and energy systems has focused on electrochemical power generating devices including salt water lithium ion pouch batteries [7], direct borohydride

fuel cells [8], hybrid battery/fuel cell systems [9], SOFCs utilizing hydrocarbon fuels [1, 10-12], and SOFCs combined with an aluminum-water reactor [3]. Salt water batteries and direct borohydride fuel cells are new technologies still in development [8]. The examples provided for SOFC systems are promising and could provide energy densities that surpass the Li-ion battery. Fuel cells offer the additional advantage of eliminating the need for mechanical to electrical conversion but may require hybridization with batteries for load following [9]. SOFCs are attractive because of their potential for achieving high thermal efficiencies and power densities [13]. This study will explore the potential for solid oxide fuel cells in UUV power plants with a non-conventional oxidizer (H_2O_2) and fuel sources (Al + H_2O to make H_2).

1.2. Solid Oxide Fuel Cells for UUVs

SOFCs can utilize H_2 fuel, reformed hydrocarbon fuels, or even light hydrocarbons as a fuel source. Unlike low-temperature polymer exchange membrane (PEM) fuel cells, which are poisoned by CO, SOFCs operate at adequately high temperature to oxidize CO as well as light hydrocarbons. Conventional low-temperature PEM fuel cells require high purity hydrogen with < 10ppm CO [14]. While SOFC systems can have high efficiencies, 50-55%, using hydrocarbon fuel [15], they must include larger balance of plant components such as steam reformers and CO_2 removal systems for UUV applications. A study by Carreiro and Burke used dodecane, $CH_3(CH_2)_{10}CH_3$, as a fuel for a SOFC system in a proposed UUV power plant, requiring steam

reforming components, heat exchangers for heat management, and a CO_2 absorber bed [1]. The size of the CO_2 absorber and fuel reformer in that study raised questions about whether a non-carbonaceous fuel source might be preferred. It was believed that the system, however, could reach a specific energy range of 400-600 Wh/kg and energy densities between 400-600Wh/L.

This study will explore an alternative fuel source to hydrocarbons, notably a metal-H_2O oxidation system that provides H_2 as fuel to the SOFC [3]. In addition, an air-independent supply of O_2 must be considered. In this study, decomposition of H_2O_2 solutions are studied as a source of O_2 for the SOFC. This study focuses on the performance of the SOFC with these alternative oxidizer and fuel source. The study explores how operating conditions (temperature and species compositions) for running a SOFC impact performance with the air-independent conditions.

1.2.1. Introduction to SOFCs

SOFCs operate at high temperatures, 500-900°C where they electrochemically oxidize fuel (hydrogen, reformate, and/or light hydrocarbons) to make electricity and some waste heat. The SOFCs are stacks of electrochemical cells each of which is primarily comprised of a membrane electrode assembly (MEA). The MEA includes the porous anode where fuel is oxidized, the porous cathode where O_2 is reduced, and the dense electrolyte where oxide ions (O^{2-}) conduct from the cathode to the anode. The O^{2-} ions conduct through the electrolyte because of a gradient in O_2 partial pressure across the membrane. On

the fuel side, the effective O_2 partial pressure is extremely low and creates a driving force (chemical potential) for O^{2-} ions to conduct through the electrolyte from the cathode to the anode. Most SOFC electrolytes are doped oxides which have relatively good ionic conductivity through defects of oxide-ion vacancies.

The electrodes contain a catalyst that encourages the charge transfer reactions to facilitate O_2 reduction on the cathode and fuel oxidation via the O^{2-} ions on the anode. At a SOFC cathode, O_2 reduction catalysts, such as lanthanum strontium manganite (LSM) or lanthanum strontium cobalt ferrite (LSCF), have been developed to incorporate O^{2-} ions that conduct through the electrolyte. A review of cathode materials can be found in earlier studies [16]. The global cathode reaction is given here:

$$O_2(gas) + 4e^-(cathode) \Leftrightarrow 2O^{2-}(electrolyte) \qquad \text{(Reaction 1.1)}$$

In the SOFC anode, nickel cermets (Ni + electrolyte composites) [17] or oxide catalysts that are stable in reducing environments such as doped strontium titanates [18] facilitate H_2 oxidation as indicated here:

$$2H_2(gas) + 2O^{2-}(electrolyte) \Leftrightarrow 2H_2O(gas) + 4e^-(anode) \qquad \text{(Reaction 1.2)}$$

Reactions 1.1 and 1.2 are charge transfer reactions often occurring at the three phase boundaries (tpb) where gas, electrode, and electrolyte meet. Electrons given off in Reaction 1.2 travel up to the next cell in the stack until they reach the final cell. From here the electrons go through an external load (resistance) only then to return to the first cell where they facilitate O_2 reduction in the first cathode of the

SOFC stack. Figure 1.2 shows a schematic of the reactions occurring within the MEA for a single cell and three cells in a stack connected to a load.

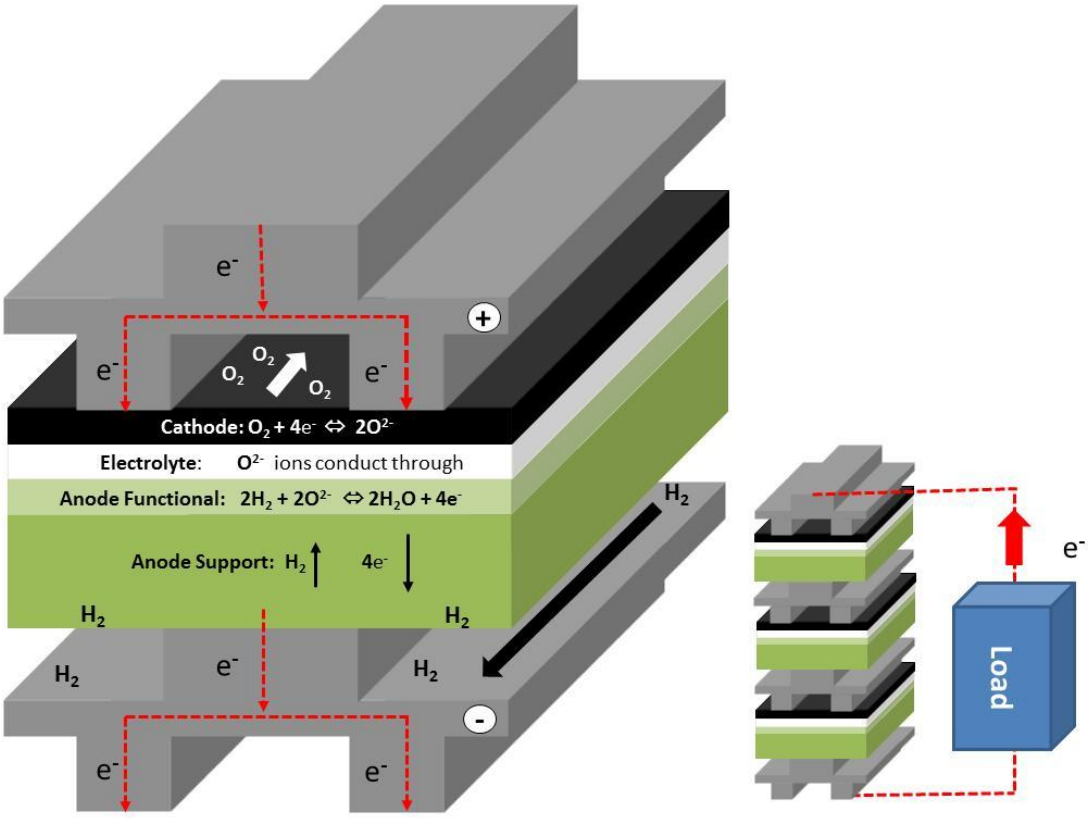

Figure 1.2 Schematic of SOFC reactions occurring at each electrode on the left and a 3 cell stack shown on the right.

Carbonaceous fuels can be oxidized in the anode, but larger hydrocarbons are broken down in the porous anode support with reforming reactions such that the electrochemical oxidation reactions at the electrolyte interface involve Reaction 1.2 and/or with CO electrochemical oxidation as shown in Reaction 1.3.

$$CO(gas) + O^{2-}(electrolyte) \Leftrightarrow CO_2(gas) + 2e^-(anode) \qquad \text{(Reaction 1.3)}$$

When using H_2 as fuel and O_2 as the oxidant, the global reaction taking place in the fuel cell is:

H_2(gas, anode) + ½ O_2 (gas, cathode) ⇔ H_2O(gas, anode) (Reaction 1.4)

If the oxidation and reduction reactions occur reversibly, thermodynamics relate the voltage between the cathode and anode through the Nernst Equation, equation 1.1, where the reversible cell voltage, $V_{cell,rev}$, is a function of the change in standard-state free energy of reaction, $\Delta G^0_{reac.}$

$$V_{cell,rev} = -\frac{\Delta G^0_{reac}}{nF} - \frac{RT}{nF} ln \prod p_k^{v_k} \quad \text{(eq. 1.1)}$$

where R and F are the gas constant (8.314 $JK^{-1}mol^{-1}$) and Faraday's constant (96485 $C \cdot mol^{-1}$), T is the fuel cell operating temperature, n is moles of electrons transferred per mole of global reaction, and p_k is the partial pressure of species k, raised to the stoichiometric value, v_k. The potential, $V_{cell,rev}$, is also known as the Nernst's potential or reversible open circuit voltage, the theoretical potential without losses. ΔG^0_{reac}, specified by equation 1.2, is the change in standard-state chemical potentials of the products and reactants of the global reaction, Reaction 1.4.

$$\Delta G^0_{reac} = \mu^0_{H_2O,anode} - \mu^0_{H_2,anode} - \frac{1}{2}\mu^0_{O_2,cathode} \quad \text{(eq. 1.2)}$$

For the global reaction, $V_{cell,rev}$ can now be written as the following:

$$V_{\text{cell,rev}} = -\frac{\Delta G^0_{\text{reac}}}{nF} - \frac{RT}{2F}\ln\left(\frac{P_{H_2O,anode}}{P_{H_2,anode}P_{O_2,cathode}^{1/2}}\right) \quad \text{(eq. 1.3)}$$

Negatively charged species have an affinity to move from anode (-) to cathode (+) through the path of least resistance. The chemical potential is a larger driving force to move the oxygen ions from cathode to anode through the electrolyte, but has no effect on electrons. Ideally the electrolyte has no electronic conductivity and very high O^{2-} ion conductivity. This forces the electrons to flow through the external circuit from the high to low potential and thus do useful work.

In practice, the actual cell voltage, V_{cell}, deviates from the reversible potential, $V_{\text{cell,rev}}$, because of resistive losses, leakage across the electrolyte, and voltage losses (or overpotentials) associated with driving the charge transfer reactions forward.

When current flows through the cell, overpotentials lower the voltage in order to drive the charge transfer reactions and necessary reactant and product transport forward to provide the current. These overpotentials (activation, ohmic, and mass transport) can occur in both the anode and the cathode.

$$V_{\text{cell}} = V_{\text{cell,rev}} - \eta_{\text{act,anode}} - \eta_{\text{trans,anode}} - \eta_{\text{act,cathode}} - \eta_{\text{trans,cathode}} - \eta_{\text{ohmic}} \quad \text{(eq. 1.4)}$$

Significant research focuses on reducing reaction rates using new electrocatalysts or electrode structures that may speed up kinetics and thereby lower η_{act}

particularly for the O_2 reduction reaction (Reaction 1.1). η_{act} can be described by the Butler-Volmer equation, eq. 1.5,

$$i = i_o \left[exp\left(\frac{\beta_f nF\eta_{act}}{RT}\right) - exp\left(\frac{-\beta_r nF\eta_{act}}{RT}\right)\right] \qquad \text{(eq. 1.5)}$$

where i_o is the exchange current density (when the current of forward and reverse reactions are equal), β_f and β_r are forward and reverse charge transfer coefficients, n is the number of electrons in the electrode reaction. η_{act} increases most significantly at low current densities (and high V_{cell}). Increasing operating temperatures decreases η_{act}, due to faster charge transfer reaction rates.

The ohmic overpotential, η_{ohmic}, is associated with the resistance of charged species, for example, electrons between electrodes and current collectors, and ions through the electrolyte. The resistance of O^{2-} conduction through the electrolyte increases with the electrolyte thickness. In equation 1.6, R_{bulk} is also known as the area specific bulk resistance (ASR) and is represented as the slope of a *V-i* curve.

$$\eta_{ohmic} = iR_{bulk} \qquad \text{(eq. 1.6)}$$

The mass transport overpotential, η_{trans}, is associated with the loss in fuel or oxidant concentration in the relevant electrode to provide adequate mass fluxes to match the ionic current density *i*. The necessary concentration gradients to match *i* lead to lower reactant concentration at the SOFC electrochemically active regions near the electrode/electrolyte interfaces. In addition the buildup of product concentration in the elctrochemically active porous anode regions contributes to

the $\eta_{trans,anode.}$ In general, η_{trans} becomes most significant at higher current densities (close to maximum). Equation 1.7 shows how η_{trans} is related to the partial pressures of reactants and products in the gas flow channels ($p_{k,a}$, $p_{k,c}$) and in the electrochemically active regions ($p_{k,a,e}$ and $p_{k,c,e}$).

$$\eta_{trans,anode} = \frac{RT}{2F} ln\left(\frac{p_{H2,a} p_{H2O,a,e}}{p_{H2,a,e} p_{H2O,a}}\right) \qquad \text{(eq. 1.7)}$$

$$\eta_{trans,cathode} = \frac{RT}{2F} ln\left(\frac{p_{O2,c}}{p_{O2,c,e}}\right) \qquad \text{(eq. 1.8)}$$

1.2.2 Material Challenges for Low-Temperature SOFCs

SOFCs are high temperature fuel cells operate at high temperatures (> 500°C) in reducing and oxidizing conditions. A popular electrolyte material is yttria-stabilized zirconia (YSZ) where ionic conduction begins to be significant at temperatures above 800°C. For operating at lower temperatures, < 650°C, various oxides have been studied for electrolytes including gadolinia doped ceria (GDC, $Gd_{0.10}Ce_{0.90}O_{1.95}$). At lower temperatures, the cost of building an SOFC system can go down with the use of alternative cheaper materials for interconnects and current collectors. SOFCs would have quicker start-up times and stacks may last longer due to less material degradation.

With their high O_2 conductivities relative to YSZ, GDC and other doped ceria materials (samarium doped ceria) can facilitate high current densities even at low temperatures. These materials are also ideal for fuel cell electrolytes because their structure does not significantly change when in reducing (Ce^{3+}) or oxidizing

(Ce^{4+}) environments. A problem arises, however, when operating at higher temperatures where the electrolyte is more likely to conduct electrons, opposing the ionic conduction, and making it a mixed ionic and electronic conductor (MIEC). This is also more apparent when the electrolyte is thin causing a low bulk resistance at the expense of lowering the OCV due to MIEC behavior in the electrolyte [19]. There can be an optimum thickness, thin enough to have insignificant bulk resistances, and simultaneously thick enough to avoid higher electronic conduction and stability of the membrane. The OCV is also affected by the density of the electrolyte. By studying scanning electron microscopic (SEM) images, the density of the electrolyte can be determined locally. SEM images were taken of fabricated button SOFCs to compare and judge the density of the material in addition to testing the cell to ensure a dense electrolyte.

In addition to the positive aspects of running at lower operating temperatures, using MIEC material for the cathode can increase the amount of active surface area for charge-transfer reactions (reaction 1.1-1.3). Also, for matching of coefficients of thermal expansion, it is common to have composite electrodes having close to 50:50 electrolyte/cathode materials. Lanthanum strontium cobalt ferrite (LSCF, $La_{0.6}Sr_{0.4}Co_{0.2}Fe_{0.8}O_{3-\delta}$) is also a MIEC cathode material that provides good O_2 reduction activity and some O^{2-} and electronic conductivity to facilitate broader regions on its surface for charge transfer reactions.

Unlike the more common lanthanum strontium manganite (LSM, $La_{0.8}Sr_{0.2}MnO_{3-\delta}$), LSCF has been shown to resist humid conditions up to 13

mol% at 700°C operating at 0.4 A/cm^2 [20], pertinent information for the current investigation of humid cathode conditions for UUV applications. The study, by Nielsen et al. tested LSM and LSCF under the same conditions of varying amounts of water vapor in the cathode oxidant stream. The LSCF voltammetry showed little change in voltage when applying 13 mol% water, while the LSM cathode showed a dramatic change in voltage under humidified oxidant streams. Reasons for the degradation were inconclusive, although Nielsen et al. attribute the passivation of voltage (recoverable decline in voltage) to silicate glassy phases deriving from some silicon oxide impurities becoming more mobile in the presence of water and more stationary in dry atmospheres. The degradation of voltage (irreversible cell damage) could occur for many reasons including new lanthanum oxide phases [21], or a change in structure that causes cracking or gas leakage thereby lowering the OCV.

The work of Nielsen et al. provided guidance in choosing LSCF as a cathode material for investigation under highly humid oxidant feeds for UUV applications with H_2O_2 decomposition as the O_2 feed source. LSCF showed resistance to humid atmospheres at 750°C, less than 13 mol% H_2O, and at 0.4 A/cm^2 while LSM showed voltage degradation. LSCF was used as a cathode to investigate a higher humidity than 13 mol% while operating at different current densities to determine a significant effect on the fuel cell's performance.

For anode-supported cells, the anode is usually split into a support and functional layer. The anode-support layer is commonly made of nickel mixed with YSZ and has a high porosity, enough to allow gas to diffuse through, but not so

much to cause instability. The anode functional layer is usually comprised of the same materials or a mixture of nickel and the electrolyte material. The functional layer is also meant to be semi-porous to allow gas to diffuse and to have sufficient contact with the electrolyte. The anode layers, like the cathode, must uphold CTE matching and increase the electrochemically active regions to promote charge transfer reactions.

1.3. Fuel and Oxidizer Requirements

To meet the desired UUV energy densities of 500 Wh/L, pure H_2 would have to be compressed to an unrealistic pressure. Cryogenic liquid H_2 has also been considered but the volume needed to contain such a system exceeds the maximum volume requirement of the UUV power section (0.47 m diameter x 1.09 m) [1]. Aluminum combustion with H_2O is another proposed method to produce H_2 [3], given by Reaction 1.5:

$$2Al(s) + 3H_2O(l) \Leftrightarrow Al_2O_3(s) + 3H_2(g) \qquad \text{(Reaction 1.5)}$$

From this reaction, approximately 18-20 L of water is needed to produce 286 kWh of hydrogen for a 40 hour UUV mission. Storing this amount of water onboard impacts the total volume of the system. However, weight and volume of the system is greatly reduced when the H_2O is recovered from the fuel cell exhaust or from water available from an oxidizer solution like hydrogen peroxide. Using an SOFC with the aluminum oxidation reactor will recycle the water by breaking it down into H_2 for the fuel cell, then joining it back to O^{-2} to form water

in the SOFC anode. There are also considerations of using sea water, although there can be many contaminants in the sea water that could affect the aluminum oxidation or corrode system components.

For air-independent UUVs, a few ideas have been proposed for storing the oxidant including liquid oxygen (LOX), lithium perchlorate, or H_2O_2 solution. There are challenges involved with all of these oxidants that would affect the system energy density, and the SOFC downstream. Similar to compressed H_2, LOX needs a cooling cycle and a preheater before the fuel cell that adds weight and volume to the system. LOX is currently being tested to be used in a PEM fuel cell system for a UUV [22]. Lithium perchlorate provides a plentiful supply of oxidant for the SOFC but it is difficult to decompose at a steady rate and the cost estimated for a single vehicle exercise cost around $10,000 [23]. The decomposition of H_2O_2 produces oxygen and significant water vapor as indicated in Reaction 1.6.

$$H_2O_2(l) + xH_2O(l) \Leftrightarrow (1 + x)H_2O(g) + 0.5O_2(g) \qquad \text{(Reaction 1.6)}$$

The H_2O_2 and H_2O in the reactants can be in either the liquid or gas phase depending on how the reaction is processed. This decomposition of H_2O_2 will produce H_2O that could be recovered and used to supply the aluminum oxidation reactor, making the system more energy dense compared to having a large water tank for storage.

1.3.1. Fuel: Aluminum Oxidation in Water

At the anode of a SOFC, water is generated from the oxidation of hydrogen. Aluminum oxidation in water will give off the products of H_2, heat, and excess water vapor that cannot be directly fed to a low-temperature (LT) SOFC because the heat would be too significant as can be seen from the heat of reaction, Δh_{reac} = -15.1 MJ/kg$_{Al}$. An inlet cooler would be needed, but there would still be enough heat to preheat the anode fuel stream. The concentration of water vapor in the fuel stream is usually regulated because for SOFCs a small amount of water vapor can be used to prevent cracking usually occurring in dry atmospheres and seen for NiO/GDC anodes [24, 25]. In the case of aluminum oxidation, the water vapor concentration will vary significantly depending on the reactor and how the aluminum oxide layer (usually forms on the surface, preventing the reaction) is removed.

Micron sized aluminum powders and nanopowders are used for Al combustion, particularly in rocket propellants to enhance the heat of combustion of other fuels for example [26]. Nano-aluminum powders have a much higher reactivity than micron sized aluminum powders due to their higher specific surface area and short reaction times. Alumifuel Inc., a company that makes aluminum canisters designed for an aluminum/water reactor, can achieve 3.12 kWh/kg of steam and hydrogen, and 3.24 kWh/L of steam and hydrogen [27]. Alternatively, there was a study by Waters et al. on the design of a UUV propulsion system that utilized an aluminum fuel seeder that suspended the aluminum powder in a H_2 flow and allowed it to react with steam. The steam was

produced by injecting water around the internal circumference of a combustor. This method prevented aluminum oxide from adhering to the walls of the combustor by solidifying the molten alumina prior to impacting the wall [3].

In this current study, humidified H_2 fuel for the anode was explored to see if there were adverse effects on the SOFC performance. Removing water prior to the anode inlet would require a condenser, removing the heat needed for anode fuel preheating, not to mention a large heat exchanger to cool the flow. This would add components to the system, effectively reducing the energy density. Varying partial pressures of dry hydrogen was also explored to demonstrate the performance with fluctuating concentrations of hydrogen.

1.3.2. Oxidizer: Decomposition of Hydrogen Peroxide

The decomposition of hydrogen peroxide as an oxidant for an SOFC provides heat from the exothermic reaction Δh_{reac} = -5.6 $MJ/kg_{H_2O_2\ Mix}$ that can be used to preheat the oxidant stream. Depending on the concentration of hydrogen peroxide in water (60 wt% used in this study) and the type of reactor used, there would be a varying amount of water vapor with the oxygen. Some studies have looked at micro packed bed reactors with 30 and 50 wt% H_2O_2 in water [28]. Since H_2O_2 readily decomposes in standard atmospheres, stabilizers are usually added to prevent decomposition during transport or if sitting for long periods of time. These stabilizers tend to be proprietary as well which makes it difficult to know what type of catalyst to use in the reactor. The most common type of catalyst seen in literature is manganese dioxide [29]. The proprietary stabilizer

and catalyst could limit the control of the rate of decomposition and, depending on the H_2O_2 concentration in water, there could be a significant amount of water vapor present in the reactor exhaust.

It has been shown (on a small button SOFC level) that water vapor could be detrimental to the SOFC cathode causing voltage degradation with increasing concentrations of water vapor [20, 30]. When left for long periods of time with concentrations of water (13 mol% H_2O), the cathode could experience permanent damage and decreased voltage.

This study investigates LSCF cathode material and operating at lower temperatures and different current densities to avoid decreased performance of a SOFC under humid conditions. Exploration of high humid conditions (40-50 % by mol) and varying O_2 partial pressure to simulate the decomposition of H_2O_2 and oxygen starvation of the SOFC will be shown in this study.

1.4. SOFC Systems Integration

At a system level perspective, LT SOFCs can bring attractive aspects to the UUV system. The system can heat up quickly thereby requiring less fuel to reduce the nickel oxide down to nickel in the anode. Using less fuel with faster start-up times adds more time to the mission. In addition to reduced cost of materials and less insulation needed, LT SOFCs should theoretically have longer lifetimes avoiding material degradation. The types of fuels proposed in previous sections incorporated into the UUV system design can also be more easily integrated when the fuel cell is operating at lower temperatures.

An example of using the aforementioned fuel and oxidant is in the study by Waters et al. combining a turbine with an SOFC hybrid, and understanding the tradeoff of bubbling or storing excess H_2 from an aluminum oxidation reaction or utilizing it as direct fuel for the SOFC. It would be more energy dense to bubble off the excess H_2, but for stealth missions, the best way to use the H_2 would be to feed it to a SOFC rather than compressing (requiring a large amount of energy) [3].

In the current design concept, shown in Figure 1.3, the system would not contain a turbine or store H_2 onboard the UUV. However, it would use aluminum as fuel and hydrogen peroxide as the oxidant. Water could be stored in a tank and a specified amount would be fed to the aluminum oxidation reactor. From the highly exothermic oxidation reactor, an anode inlet cooler must be upstream of the fuel cell. The anode inlet cooler would preheat the cathode inlet through a heat exchanger.

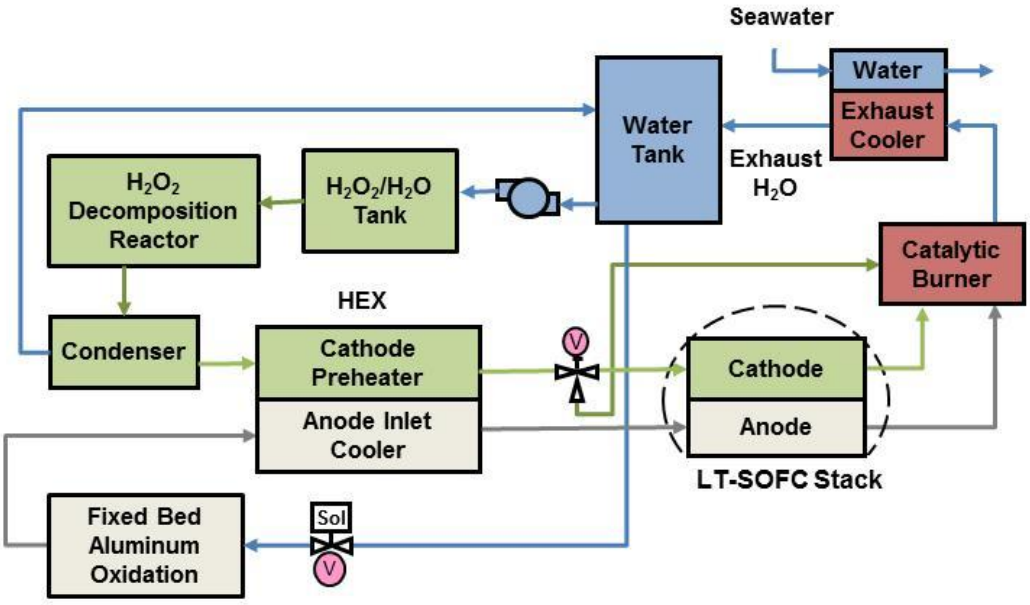

Figure 1.3 Schematic of proposed Al/H_2O_2 system design incorporating an exhaust cooler downstream of the aluminum oxidation reactor, a condenser downstream the H_2O_2 decomposition reactor, and heat exchanger between the cathode and anode inlet gases prior to entering the SOFC stack. After the SOFC, a catalytic burner is used to provide additional exhaust water to the storage tank. Seawater is used to provide cooling and a continuous recycled water stream provides water to the aluminum oxidation reactor.

On the oxidizer side, H_2O_2 stored in water at a certain percentage of weight in water would be pumped into a decomposition reactor that could use a catalyst to speed up the reaction or heat the H_2O_2 to increase the rate of decomposition. The next proposed step includes a condenser, condensing the water out of the oxidant stream. This step would remove most of the water (~90%) and the resultant O_2 + H_2O mixture would have to be preheated. Cathode and anode exhaust streams could be reacted in a catalytic burner, and that exhaust water could be stored in a tank and used for feeding the aluminum oxidation reactor as needed.

Removing a few components could make a significant impact on the feasibility of the design. To ensure that the performance of the fuel cell will not be affected, given a proper set of operating conditions and material requirements, this study will explore the potential of flowing depleted and humidified fuel and oxidant feeds to a lower operating temperature SOFC to simulate the air-independent fuel reactors integrated into this systems.

1.5. Objectives and Thesis Outline

This study explores lower operating temperature SOFC materials, microstructure, and fuel cell performance under humidified fuel and oxidant streams while operating at a range of potential conditions relevant for UUV applications. SOFC materials such as GDC and LSCF which can operate at temperatures at or below 650°C were used to fabricate button-cell SOFCs to experimentally test cell performance at various operating conditions expected to be experienced in an SOFC operating as a UUV power generator. The effects of fuel depletion with humidified H_2 for the anode and oxidant depletion with humidified O_2 for the cathode were explored with the button cell tests. Testing individual button cells provides clearer insight into how cell materials and microstructure impact performance. Results from button cells scaled to a 2.5 kW stack size is a preliminary basis for assessing LT SOFC operation utilizing H_2 fuel from aluminum oxidation and O_2 oxidant from decomposition of H_2O_2.

Detailed descriptions of the fuel cell fabrication and testing methodologies are given in Chapter 2. This chapter also presents the different electrochemical

testing techniques used on button fuel cells such as linear sweep voltammetry and electrochemical impedance spectroscopy. Chapter 3 presents the results of these tests and includes results from cell stability tests with humidified fuel and oxidant environments. Humidified tests provided insight into the trade-offs between high efficiency versus high fuel cell power density (W/cm^2).

Chapter 4 uses these results to assess approximate stack size requirements for an SOFC stack in a prototype UUV system. Results from button cell testing were scaled to a SOFC stack to estimate fuel cell inlet flow rates and temperature. Knowing the reactant amount for the fuel cell, Al/H_2O and H_2O_2/H_2O weights and volumes were calculated to provide insight on the energy density of the system based on SOFC operating conditions for particular UUV missions.

Chapter 2: Experimental Procedure

SOFC button cells are tested in this study over a wide range of fuel and oxidizer conditions and operating conditions in order to assess local stack performance as a function of fuel and/or O_2 depletion. This chapter provides details on the SOFC button cell fabrication for the anode, electrolyte, and cathode. Iterative fabrication provided insight on best practice and solutions to challenges. The test rig and testing methods for these button cells are also described in this chapter. Approaches to cell conditioning and stability testing under various reactant depletion and cathode and anode humidity are discussed. Button cell performance was regularly characterized with linear sweep voltammetry (LSV) and electrochemical impedance spectroscopy (EIS).

2.1. SOFC Button Cell Fabrication

Anode-supported SOFC button cells were fabricated for the experiments in this study with a composite anode functional layer, dense electrolyte, composite cathode layer, and silver current collectors. Figure 2.1 is a representation of a cross-section of the button cells fabricated in this work, showing the layers of the cell. Each layer of a button fuel cell requires unique fabrication steps and there are different ways to approach those steps. These include tape casting and uniaxial pressing of powders for the anode support layer; drop-coating, spin coating, and pulsed laser deposition for the anode functional and electrolyte layers; and painting and dip coating for the cathode layer. In this study, 2 cm diameter button cells described below contain uniaxially pressed

anode support layers, drop-coated anode functional layers and electrolytes, and painted cathodes and current collectors. Table 2.1 contains the compositions and characteristics of each layer.

Table 2.1 List of the four layers of the baseline SOFC button cells with composition, thickness, and porosity.

Layer	Composition	Thickness (μm)	Porosity (%)
Anode support	$Ni/(Y_2O_3)_{0.08}(ZrO_2)_{0.92}$ **(Ni/YSZ)**	1,000	58
Anode functional	$Ni/Gd_{0.1}Ce_{0.9}O_{1.95}$ **(Ni/GDC)**	15-20	25
Electrolyte	$Gd_{0.1}Ce_{0.9}O_{1.95}$ **(GDC)**	10-15	Dense
Cathode	$La_{0.6}Sr_{0.4}Co_{0.2}Fe_{0.8}O_{3-\delta}$ $/Gd_{0.1}Ce_{0.9}O_{1.95}$ **(LSCF/GDC)**	20-50	85
Current collector	Ag paste/Ag mesh	~50	~50

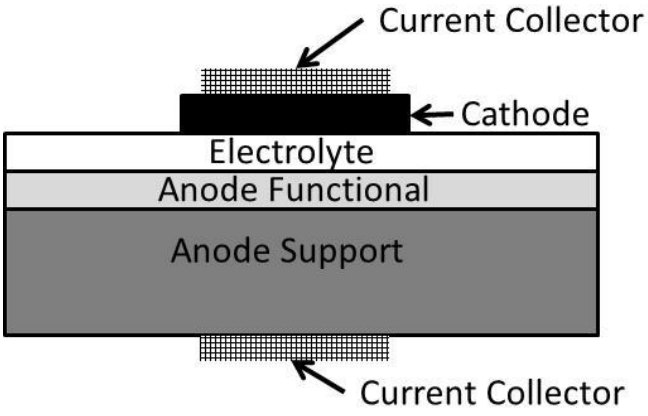

Figure 2.1 Representation of SOFC button cells used in experiments with the anode support, anode functional layer, electrolyte, cathode and two current collectors.

2.1.1. Characterization of Material Powders

To control the fabrication procedure and maintain consistent button cells, raw materials must be characterized to ensure correct surface area and particle size. For surface area, BET measurements were taken with a Micrometrics Instrument for the $Gd_{0.1}Ce_{0.9}O_{1.95}$ (GDC-10 TC grade, and nano grade from Fuel Cell Materials) and $La_{0.6}Sr_{0.4}Co_{0.2}Fe_{0.8}O_{3-\delta}$ (LSCF powders also from Fuel Cell Materials) to verify the surface area specified by the vendor. The BET measurements showed all surface areas were within specifications. The particle sizes were confirmed in SEM images and all samples taken showed the particles having consistent diameters specified by the vendor. Each section following will have a more detailed description of the powders used and their characteristics. Particle size and vendors are listed in Table 2.2.

Table 2.2 List of materials used in SOFC button cell fabrication with characterized surface areas in bold.

Material	**Particle Size (μm)**	**Surface Area (m^2/g)**	**Vendor**
Nickel Oxide (NiO)	44	-	Fisher Scientific
Graphite Pore Former Timrex KS-4	4	26	Timcal
Yttria Stabilized Zirconia TZ-8YSB(YSZ)	0.14	7 ± 2	Tosoh
Gadolinia Doped Ceria (GDC-TC)	0.1-0.5	**5.3 ± 0.17**	Fuel Cell Materials
Gadolinia Doped Ceria (GDC-nano)	0.005-0.010	**182 ± 11**	Fuel Cell Materials
Lanthanum Strontium Cobalt Ferrite (LSCF-P)	0.3-0.5	**4.4 ± 0.1**	Fuel Cell Materials

2.1.2. Anode Support

A thin and highly porous support layer is preferred to reduce gas diffusion losses provided it can maintain adequate durability as a support. To control the porosity, pore formers which are burned out in the high-temperature firing step, are added to the support powders before being pressed into a disc and fired in air. In this study, Timrex KS-4, 4 μm particle size graphite powder from Timcal served as the pore former. These pore formers burn out during heating to 900°C [31], which is low enough not to significantly sinter the support. The thickness of the support layer was controlled with the amount of powder pressed in a uniaxial press. Controlling the porosity and thickness of the support prevented mass transport loses when testing the button cell.

Nickel oxide (NiO) powder from Fisher Scientific with particle size 44 μm, and Yttria Stabilized Zirconia (YSZ, grade TZ-8YSB) powder from Tosoh Corporation with particle size 0.14 μm were mixed in a ratio of 70% NiO and 30% YSZ by weight in a ball mill with isopropanol for 24 hours. The Timrex graphite pore formers were added to the anode-support mixture and ball milled for 2 more hours. The slurry was dried, and the resultant powder sifted through 90 μm, and then pressed in a hydraulic press at 7 metric tons for 10 min inside a 3 cm diameter die. The resultant disc was heated in a furnace up to 900°C, ramping at 1.5°C/min, and held there for 3 hours before ramping back down at the same rate to room temp. At this heating schedule, the graphite powder was burned out to make the porous anode support layer.

When the support layers were placed in the furnace, one alumina plate was set on the top and one on the bottom of each support to ensure that the cell stayed flat throughout the heating process. The thickness of the support layer was about 1000 μm thick with a porosity calculated to be 58% after sintering (in the electrolyte step) and reducing the NiO to Ni (before testing). Experimental results shown by Zhao and Virkar displayed minimum mass transport overpotential for Ni/YSZ supported cells with porosities between 57% and 76% [32]. At high porosities, 70-80%, the anode support layer is susceptible to cracking due to high stress concentrations near the pores in the ceramic structure.

2.1.3. Anode Functional Layer

The anode functional layer provides the electrocatalytic active region where fuel (H_2 here) is oxidized at the tpb interfaces where the fuel, electrolyte, and electrode catalyst come together. The anode support layer must also provide good matching of coefficients of thermal expansion (CTE) with the electrolyte and the porous electrode. In this study, the anode functional layer was composed of Ni, and GDC. The linear CTE for Ni and GDC are respectively $14 \cdot 10^{-6}$ K^{-1} [33] and$12.5 \cdot 10^{-6}$ K^{-1} [34] at 600ºC. The functional layer performs best with the maximum amount of tpb for promoting the charge transfer reaction. At low effective oxygen partial pressures associated with the fuel electrode, the GDC electrolyte material exhibits mixed ionic-electronic conductivity at the highly reducing conditions of the anode. The MIEC behavior increases the electrochemically active regions on the exposed GDC surface beyond the actual

three-phase boundary interfaces with the Ni [35]. The porous functional layer with its network of GDC particles allows for O^{2-} to conduct up in through the depth of the functional layer to provide more active regions for the charge-transfer reactions. The functional layer typically uses a lower porosity compared to the anode support layer to increase O^{2-} conduction three-phase boundary intersections to facilitate charge transfer reactions.

The anode functional layer powder was prepared similarly to the anode support layer powder, but without graphite pore former. Reduction of the NiO provided enough porosity for the gas to diffuse and react in the thin functional layer. Polymer binder was also added to the functional layer slurry, and the binder was removed during heating and provided a small amount of porosity after burnout during the heating process. To make the functional layer coatings, NiO with particle size 44 μm, GDC TC-grade powder with particle size 0.1-0.5 μm, and GDC Nano Powder with particle size 5-10 nm were mixed in a ratio of 60% / 35% / 5% by weight respectively, in a ball mill with isopropanol for 24 hours. The nano-sized GDC powder improved the conduction pathways in the functional layer porosity, and thereby increased tortuosity.

After the NiO/GDC slurry was dried, the powder was sifted through 90 μm. This powder was formed into a slurry with additives to drop-coat (small droplets of slurry by pipette until it completely covered the surface) onto the anode support layer. For each cell, NiO/GDC powder was mixed with isopropanol, dispersant KD-1 (Tape Casting Warehouse) used to separate the particles, and binder, poly vinyl butyral (PVB), used to “coat” the particles and

ultimately keep the powder from settling in solution. The weight percentages of each component are shown in Table 2.3.

Table 2.3 Anode Functional Slurry Composition

Step	Component	Wt% of NiO/GDC	Amount per batch
1	Isopropanol	90	4.6 ml
	KD-1	1	0.004 g
2	NiO/GDC TC and Nano Mix	-	0.4 g
3	Isopropanol	66.3	1ml
	PVB	2.4	0.01 g

Approximately 700 µl of the functional layer slurry was evenly distributed over the anode-support layer surface using a pipette (referred to in this work as 'drop-coating'). The functional layer dried for at least 12 hours in room-temperature air before heating in the furnace at the heating schedule shown in Figure 2.2. Two alumina plates are placed on top and one alumina plate on the bottom of the cell while heating in the furnace to keep the cell flat during heating. Even without graphite pore former, the porosity of the functional layer was calculated to be ~25 $\pm$ 0.4% after sintering (electrolyte heating) and reduction of NiO to Ni. The thickness of the functional layer, with this method of drop-coating, was measured to be 15-22 µm after sintering.

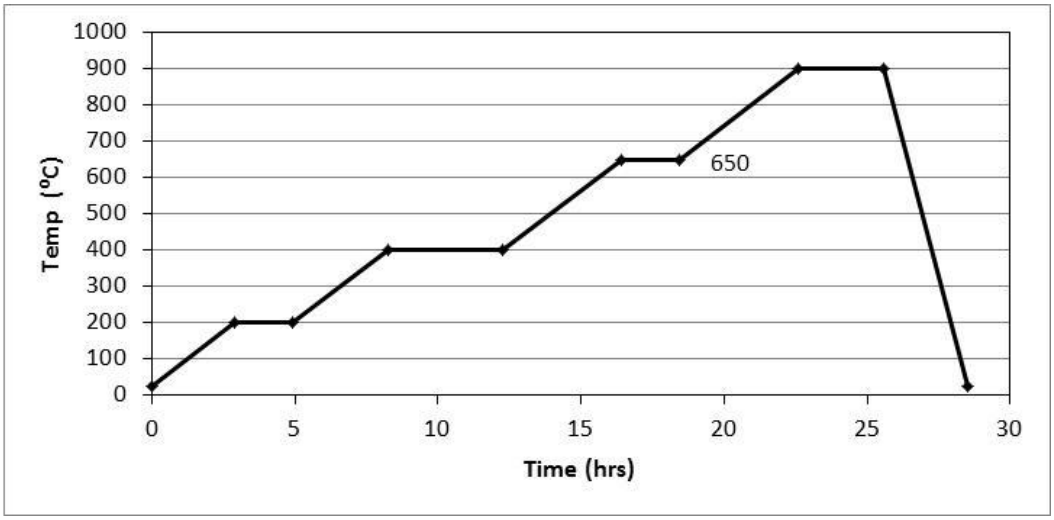

Figure 2.2 Anode functional layer heating schedule

2.1.4. Electrolyte

Operating at higher temperatures, GDC has a deleterious transport of electrons through the electrolyte, due to its MIEC quality. This causes GDC to have leakage currents across the electrolyte which lowers the OCV by shorting some amount of the electrolyte. The leakage current depends on temperature, electrolyte thickness, and the electrical potential across the electrolyte as seen in a study by Wachsman et al. investigating the electrolyte thickness and its effect on the OCV [19]. For electrolytes with MIEC behavior under reducing conditions, OCV increases with electrolyte thickness, but increasing electrolyte thickness also increases electrolyte ohmic resistance. Dense GDC electrolytes, 5-10 μm thick provided the optimal powder density based on the tradeoff between higher OCV and higher ohmic resistance. In the case of a porous electrolyte, gas leaks across, causing the cell OCV to decrease. Also, H_2 oxidation raises the likelihood of

electrolyte cracks due to thermal expansion. The fabrication method of the electrolyte for this study attempted to meet both a high density and relatively small thickness to maximize the OCV.

The electrolyte was fabricated with a similar drop-coating method as the anode functional layer. Table 2.4 shows the composition of the prepared electrolyte slurry. KD-1 dispersant was sonicated in isopropanol, then GDC powder TC-grade was added to the solution and sonicated for 20 more minutes. The resultant slurry was ball milled for 168 hours in a high-density polyethylene (HDPE) bottle with zirconia beads. PVB and polyethylene glycol (PEG), used as a plasticizer, were added to the slurry and sonicated for 30 min. Each electrolyte layer consisted of about 700 µl of slurry per cell. Using scanning electron microscopy (SEM), the thickness of the electrolyte was measured to be in the 8-12 µm range.

Table 2.4 Electrolyte Slurry Composition

Step	Component	Wt% of NiO/GDC	Amount per batch
1	Isopropanol	88	4.6 ml
	KD-1	1	4.8mg
2	NiO/GDC TC and Nano Mix	-	480mg
3	Isopropanol	62	1ml
	PVB	8	44 mg
4	Isopropanol	62	1ml
	PEG	5	26mg

After the slurry was dropped onto the anode functional layer, the electrolyte layer was dried in air at room temperature for at least 12 hours. The

sintering temperature and schedule are crucial for achieving electrolyte density. The heating schedule shown in Figure 2.3 first sits at 400 and 500°C to slowly burn out the PVB binder [36] and PEG plasticizer [37] before going up to 900°C to remove any carbon. A dense electrolyte was seen when sintered to 1450°C. When the cell was heated in the furnace, approximately 21-22 g of alumina plates were stacked on top to apply a uniform pressure on the cell so it sintered as a flat button. After sintering, the cell diameter shrunk to about 70% of its original diameter.

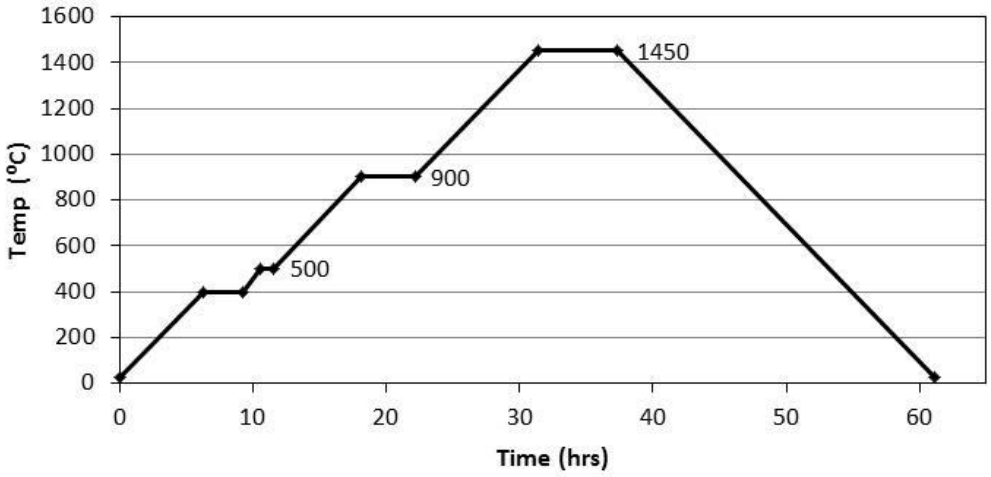

Figure 2.3 Heating schedule for sintering electrolyte.

Formation of truly dense GDC electrolytes depended on many factors including: time for ball-milling electrolyte particles, the amount of binder and plasticizer added, the electrolyte sintering time and temperature, and the weight applied to the cell during sintering. SEM images in Figure 2.4 (A and B) of cells made with 12 wt% PVB and 7 wt% PEG show unacceptably porous electrolytes

after ball-milling the electrolyte slurry for 5 hours and sintering at 1500°C while applying greater than 35 g of pressing force on top of the cell. After changing the amount of PVB to 8.4 wt%, PEG to 5 wt%, the heating schedule to a slower ramping rate (shown in Figure 2.2), the amount of pressing force while sintering (~21grams per cell), and ball-milling for 168 hours, the electrolytes were quite dense, Figure 2.5. The resultant OCV for each of these cells corresponds to the apparent densities seen in Figure 2.4 and 2.5. The highly porous electrolyte had an OCV of 0.4 V at 600°C compared to the cell with a more dense electrolyte had an OCV of 0.8 V at the same temperature. The influence of electrolyte density on OCV can be seen in the Nernst Equation (eq. 1.2). The partial pressure of oxygen lowers as O_2 gas leaks across a porous electrolyte and combines with H_2 fuel at the anode to make H_2O, lowering the total OCV.

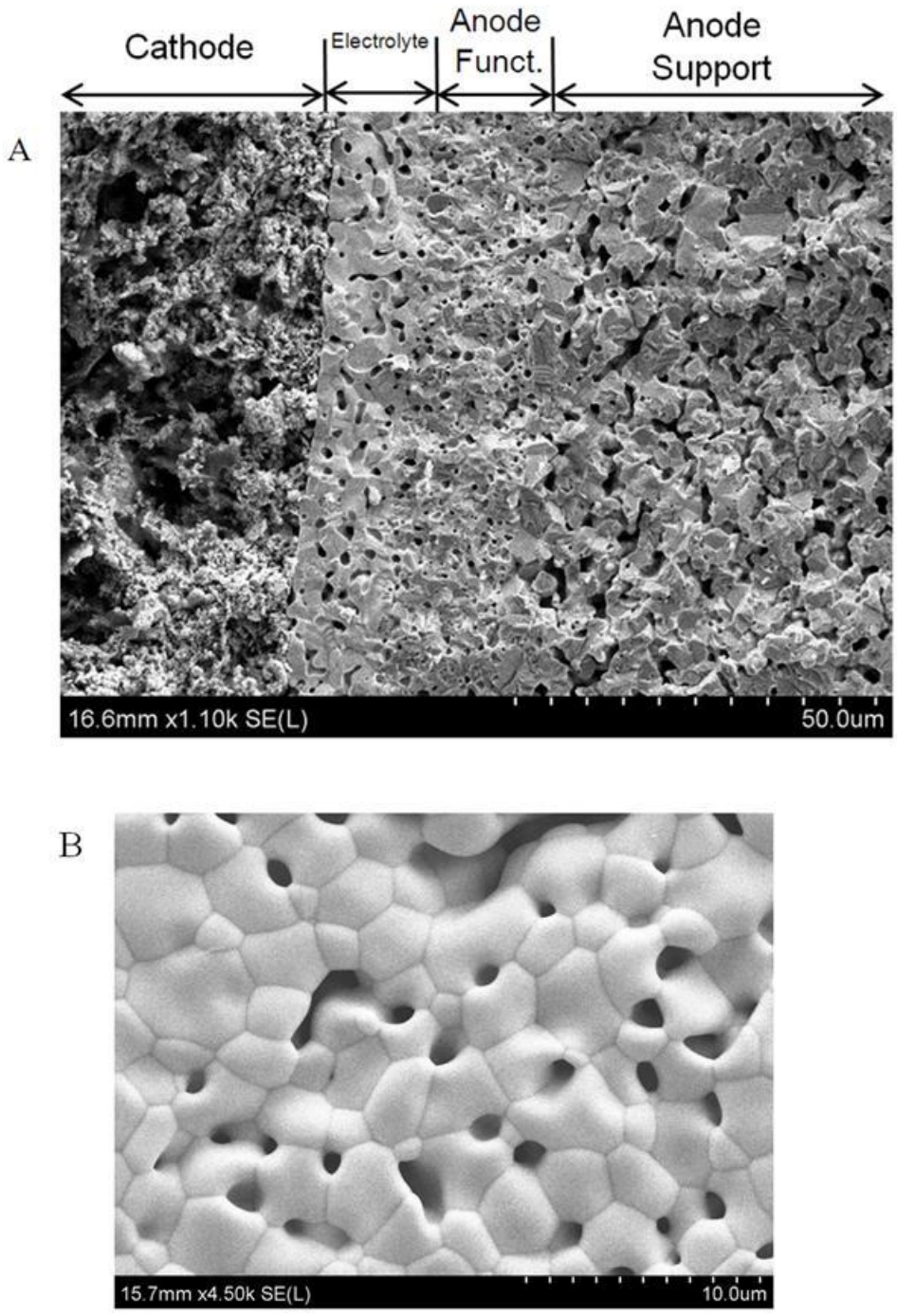

Figure. 2.4. A.) SEM image of the fabricated button SOFC cross-sectional view of the electrolyte with higher porosity due to 12 wt% of binder, 7 wt% plasticizer, and 5 hours ball milling time (sintered at 1500°C). B.) Topical view of same electrolyte.

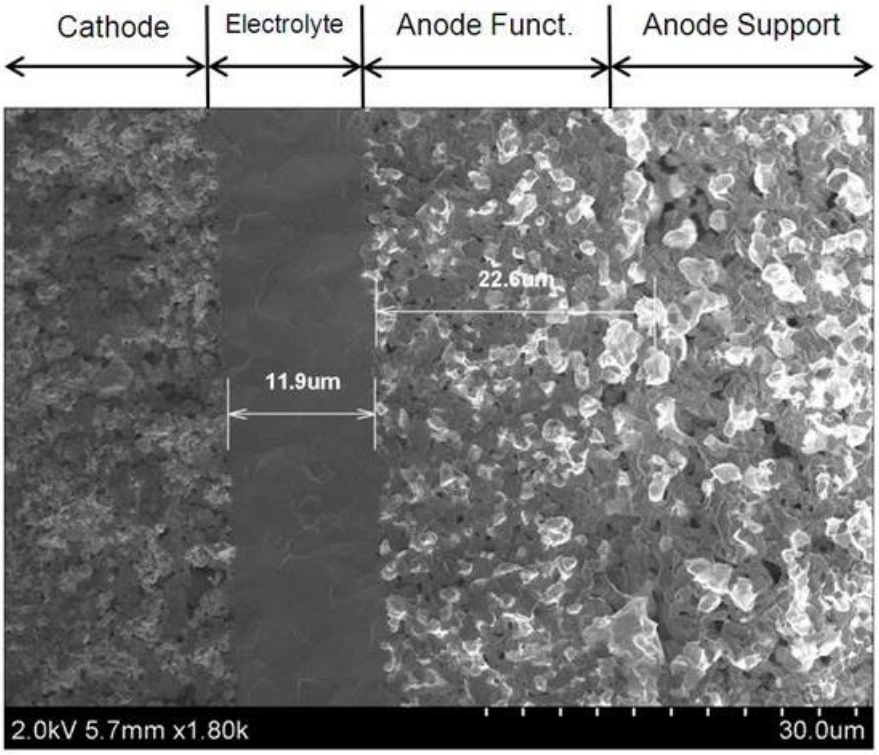

Figure 2.5 Cross-sectional view of button cell with electrolyte containing 8.4 wt% binder, 5 wt% plasticizer, and a ball milling time of 168 hours (sintered at 1450°C).

The porous images shown in Figures 2.4 A and B suggest something hindered the electrolyte particles from sintering. The possibility of gases other than O_2 generated during binder decomposition being trapped inside the electrolyte as it sintered is highly likely. A reduction of binder and the amount of weight pressed on the cell could have mitigated this porous electrolyte problem. Burning out the polymer at a slower rate may have had an impact on this as well.

The ball milling procedure was used to reduce the amount of agglomerates in the slurry, but may have reduced the particle size. This could affect the rate at

which the ceramic will sinter and shrink. For finer particles, the cell would shrink more than it would with larger particles, although finer particles tend to agglomerate due to electrostatic and surface forces, causing pores to form during sintering [38]. An experimental study by Maca et al. [39] showed that a GDC particle size of about 20 nm caused a high porosity after sintering. The powders used in this study had a starting particle size of 0.1 - 0.4 μm and SEM images of electrolytes using particles after ball milling for 168 hours showed a similar range in size. Keeping the nanoparticles suspended proved difficult with limited amount of binder. Electrolyte sintering tests were performed for a range of PVB binder 8-20 wt% in the electrolyte slurry to make it uniform. Complete oxidation of the polymer during sintering and gas removal was best achieved by heating slowly to 900°C to burn out the polymer before the GDC particles started to sinter together.

The sintering temperature was chosen to be 1450°C because the resultant cells achieved a dense electrolyte and a max power density of 0.46 W/cm^2 at 650°C. The amount of weight pressing on the cell had to be enough to keep it from deforming while sintering. 22 g of weight (corresponding to an approximate compressive stress of $3.3 \cdot 10^{-3}$ kPa) provided a compromise that did not restrict shrinking of the electrolyte. Ball milling the electrolyte slurry for one week was assumed to be ideal to break down the agglomerates in the electrolyte solution. A reduction of PVB binder to 5 wt% of GDC powder also proved beneficial to increasing electrolyte density in addition to increasing the time needed to burn the binder out of the electrolyte.

2.1.5. Cathode

Like the anode, the cathode must be porous to allow for gas diffusion. In addition, the cathode must have a highly active layer near the electrolyte for O_2 reduction. Because O_2 reduction is generally the largest overpotential in the SOFC, the cathode layer is made thin relative to the anode in order to minimize losses in O_2 partial pressure due to transport through the porous cathode. Losses in O_2 partial pressure further increase cathode overpotentials.

In this study, a thin mixture of lanthanum strontium cobalt ferrite (LSCF, $La_{0.6}Sr_{0.4}Co_{0.2}Fe_{0.8}O_{3-\delta}$) and GDC formed the cathode. LSCF was chosen as the electrocatalyst because of its higher O^{2-} conductivity and activity at temperature < 700°C [40]. The cathode was made without the use of pore formers. Instead, polymeric additives in the cathode paste burned off during firing to create a porous structure (about 50% porosity). LSCF P-grade powder (Fuel Cell Materials) with particle size 0.3 - 0.5 µm was mixed with GDC TC-grade powder in a weight ratio of 50:50, to make the cathode. The GDC mixed into the cathode ensures a better CTE match with the electrolyte and extends the electrolyte/electrocatalyst interface. A weight ratio of 50:50 or 40:60 LSCF/GDC compositions have been known to provide a lower polarization resistance than pure LSCF, 60:40, and 30:70 ratios of LSCF/GDC mixtures [41].

The cathode powders were combined with a plasticizer, terpineol, 40 wt% of LSCF/GDC powders, and mixed in an amalgamator for 4 min to make the paste. A 9.5 mm diameter circle was cut out of Kapton tape (50 µm thick) and adhered to the top of the electrolyte as a mask to apply the cathode paste. SEM

images showed about a 20 µm thickness after sintering at 1100°C. After the paste was dried the Kapton tape was removed and the cell was left to dry completely for at least 12 hours. The cathode was then fired at the heating schedule in Figure 2.6.

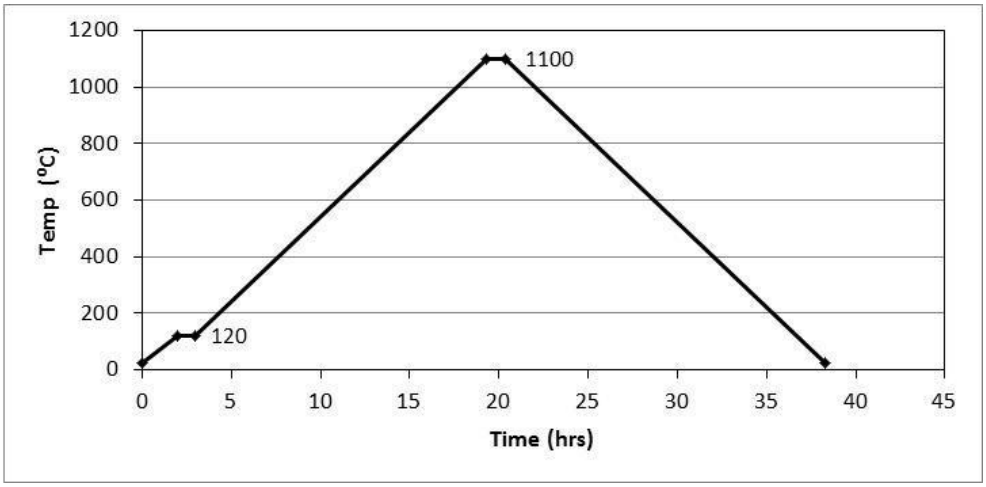

Figure 2.6 Cathode heating schedule for sintering.

2.1.6. Current Collectors

After firing the cathode, current collectors were applied on the outer faces of both electrodes, seen in Figures 2.7 and 2.8. The anode current collector was comprised of a silver wire (0.5 mm diameter) spot welded in between a nickel tube (anode gas feed tube) and nickel mesh (40 mesh, 0.13mm diameter, Alpha Aesar). The center of the silver wire was spot welded to a silver mesh (50 mesh, 0.0764mm diameter, Alpha Aesar) and attached to the anode using a porous silver paste (Fuel Cell Materials), seen in Figure 2.7. The nickel tube acted as an interconnect running out of the furnace and connected to the electrochemical testing station leads.

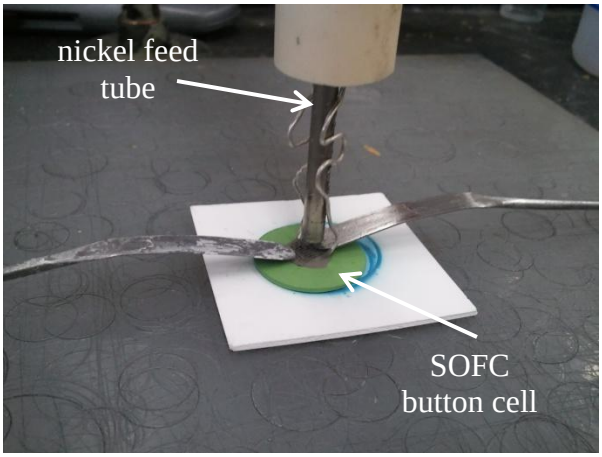

Figure 2.7 2-cm diameter button cell with anode current collector drying before the cell is pasted to the alumina tube.

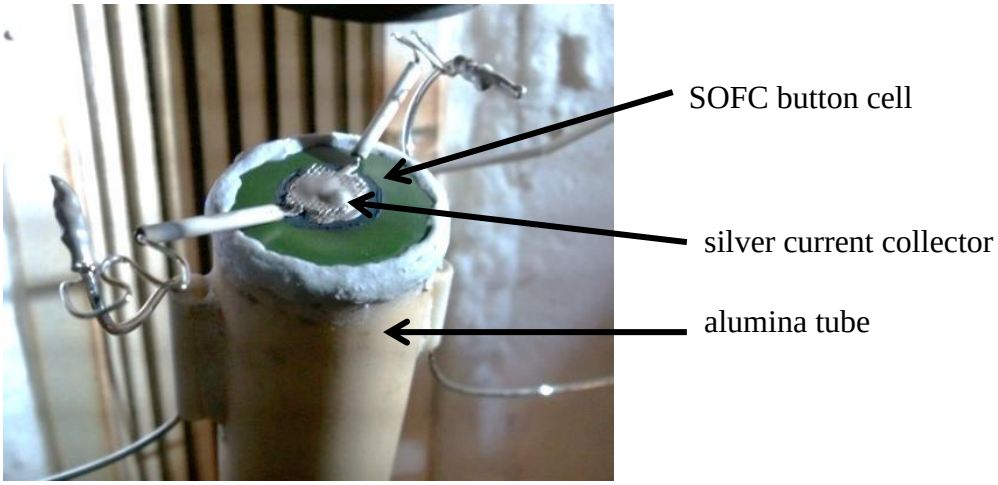

Figure 2.8 Cathode current collector after cell is pasted to the alumina tube.

After pasting the cell to the alumina tube with Ceramabond 571 (Aremco) and left to dry for at least 12 hours, the cathode current collector was attached. A 0.5 mm diameter silver wire (Alpha Aesar) and mesh were spot welded together and pasted with silver paste to the cathode. As seen in Figure 2.8, the 0.5 mm diameter silver wires were attached with silver paste to 1 mm diameter silver

wires (Alpha Aesar) to extend outside the furnace to attach to the electrochemical testing station leads.

2.2. Experimental Test Rig

The button cells were tested in a vertical tubular furnace mounted on a T-slot frame. Two alumina outer tubes were used to support the cell and hold the oxidant and fuel feed tubes in place. The anode side of the cell was pasted to the bottom alumina outer tube with Ceramabond 571, providing a proper seal between the fuel and oxidant sides. The cathode side of the cell was left to open air although a feed tube of air flow as discussed below provided an active flow to the surface of the cathode. The nickel anode fuel feed tube (4.8 mm ID) was placed so that the end of the tube was roughly 3 mm from the porous silver current collector on the anode side. This was done to make sure the fuel had a direct path to the anode. The same procedure was done to the alumina oxidant feed tube (see Figure 2.9 and 2.10). The cathode side contained a gas directive piece to ensure the oxidant gas flowed completely across the cathode active area. The alumina outer tube on the fuel side was plugged at the opposite end from where the cell was pasted to provide a small amount of backpressure to the anode side. Two small holes were drilled into the plug to allow for the feed tube and exhaust tube to leave the outer tube.

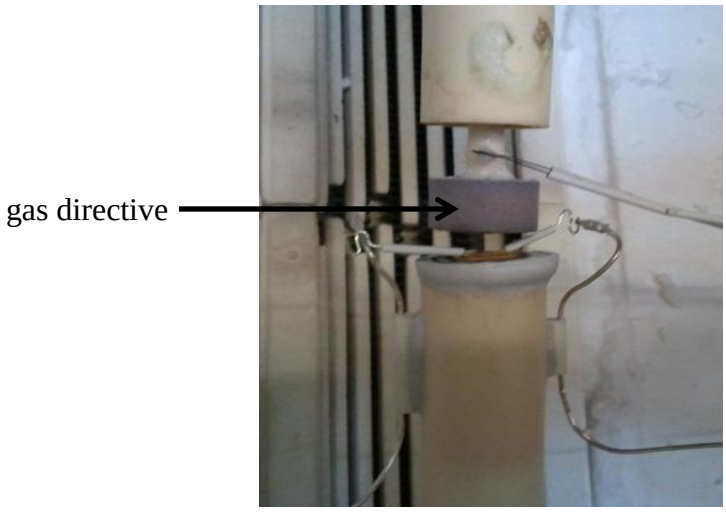

Figure 2.9 Close up view of the fuel cell pasted to the alumina tube, silver wire lead to cell (covered with an alumina insulation), and thermocouple above gas directive.

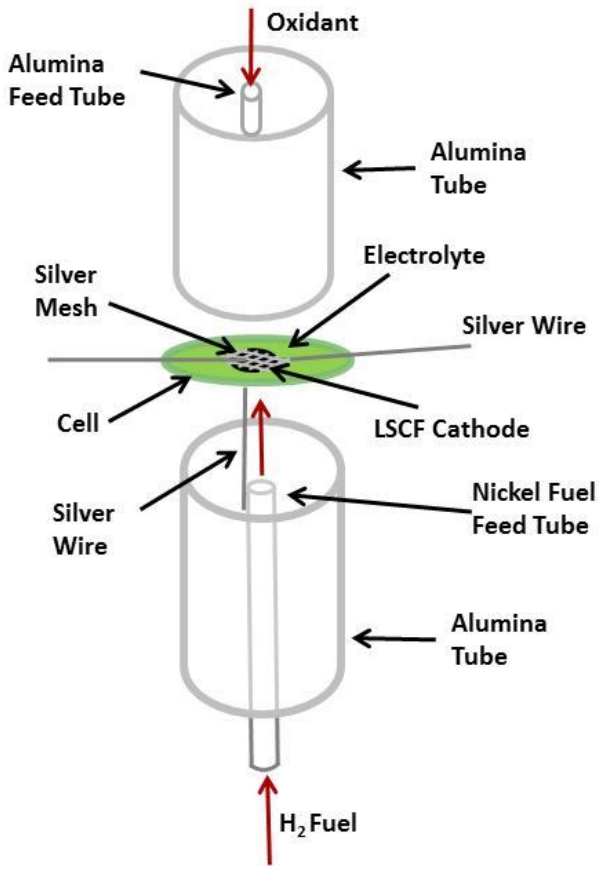

Figure 2.10 Rig design diagram for cell tests.

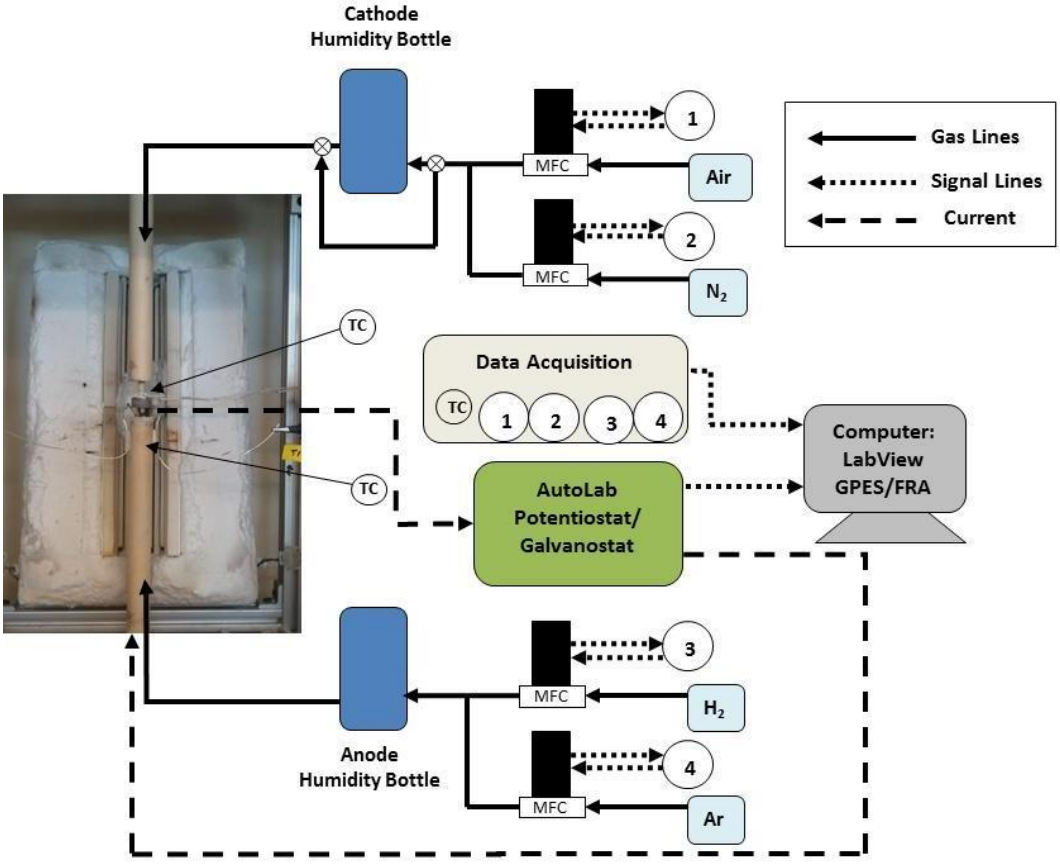

Figure 2.11 Experimental set-up with the gas lines to the cell, signal lines for data acquisition and control of MFCs.

The experimental set-up diagram is illustrated in Figure 2.11. Temperature and flow rates were monitored and controlled using National Instruments (NI) LabView program. K-type thermocouples (Omega) and Brooks mass flow controllers (MFCs) were connected to a NI data acquisition DAQ system with SCXI 1000 chassi and converter modules. Gas flowed through humidity bottles on both the cathode and anode sides to simulate the decomposition of hydrogen peroxide (for the oxidant) and aluminum oxidation in water (for hydrogen fuel

production). Gas lines were heated between the humidity bottle and the furnace to ensure water would not condense on the gas tubes. The cell leads were connected to an electrochemical instrument, Autolab (Metrhom) potentiostat galvanostat (PGSTAT), with the cathode as the working electrode and the anode as the counter electrode. There was no reference electrode used in these experiments. The Autolab contained Brinkmann's Frequency Response Analyzer (FRA) software for EIS measurements and General Purpose Electrochemical System (GPES) software for LSV and amperometry measurements.

2.3. SOFC Testing

2.3.1. SOFC Conditioning

Ni/YSZ anode-supported button cells with a Ni/GDC functional layer, GDC electrolyte, and LSCF cathode were tested to ensure fabrication consistency and durability. All of the experimental button cells were conditioned with the following procedure prior to testing:

1. Heat cell to 100°C (without gas flow) and let sit for two hours to allow Ceramabond 571 paste to cure and seal the cell to the alumina tube.
2. Continue heating cell to 650°C up to 2°C/min while applying an anode gas flow of H_2 and Ar at 15 sccm and 90 sccm, respectively. The anode gas flow was sent through a bubbler to supply about 3 mol% water to the cell. This is done to prevent the anode from cracking [24, 25].

3. Maintain these conditions at 650°C for 24 hours to allow the NiO in the anode to fully reduce to Ni.
4. Increase gas flows to 30 sccm H_2, 30 sccm Ar, and 60 sccm air at the cathode. Let the cell stabilize at these conditions for at least 1.0 hour.
5. Begin running a potentiostatic (keeping the voltage constant) test at about 0.7V to see the corresponding current density. This ensures that the cell will not start operating in reverse if the current specified allows the voltage go below zero.
6. Run chronopotentiometry (constant current with voltage changing over time) for 12-24 hours with the current specified so that the cell initially sits at 0.7 V.
7. Perform LSV and EIS curves to look at the range of current density and to see where overpotentials are significant.

When not running tests, the cell was operated between 0.7 - 0.75 V to minimize the risk of Ni oxidation in the anode.

2.3.2. Linear Sweep Voltammetry (LSV)

LSV tests were used investigate the overall performance of the cell. A step potential of 0.01 V was applied to the cell while the corresponding current was recorded. The voltage started at OCV, usually about 0.8 V, and went down to 0.2 volts. It is important not to let the voltage get too low as you can oxidize the nickel in the anode of the cell, causing irreversible damage to the cell. The data is shown in a voltage vs. current density graph (*V-i* curve) shown in Figure 2.12.

Current is displayed as the specific current density (per area of the cathode) with units A/cm^2. The resulting power density (W/cm^2) is often shown on the same graph on a secondary axis ($\dot{W} = Vi$). The slope of the *V-i* curve is associated with the ohmic overpotential or area specific resistance (ASR).

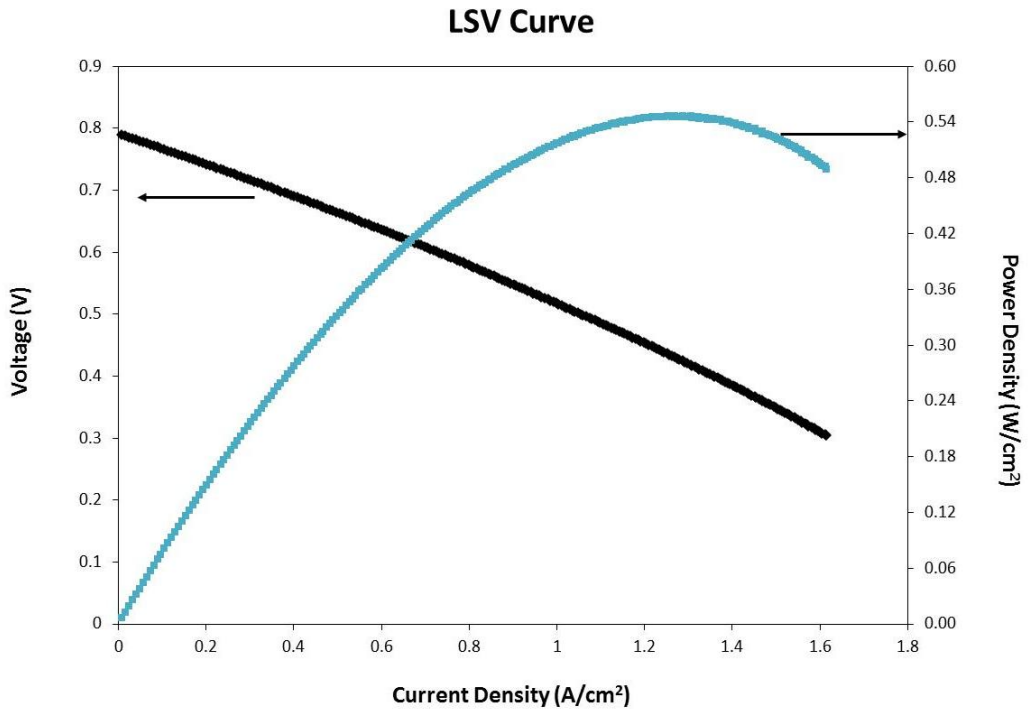

Figure 2.12 Example of LSV (*V-i* graph) graph showing cell voltage decreasing with increasing current density and the resulting power density. Testing conditions: 650ºC, 50/50 H_2/Ar with 3% H_2O at anode, dry air at cathode.

2.3.3. Electrochemical Impedance Spectroscopy (EIS)

EIS measurements allowed further understanding into the characteristics of the cell, particularly the impedances associated with structure of the electrodes and electrolyte. In this study, the frequency response analyzer (FRA) was

operated in a constant voltage (potentiostatic) mode with a controlled alternating voltage signal, V_{AC}, with frequency ω, overlaid on a constant DC voltage V_{DC}.

$$V_t = V_{DC} + V_{AC}\sin(\omega t) \qquad \text{(eq. 2.1)}$$

The measured current response is a combined constant I_{DC} with an oscillating current I_{AC}. The current response may be shifted by the phase angle, φ.

$$I_t = I_{DC} + I_{AC}\sin(\omega t + \varphi) \qquad \text{(eq. 2.2)}$$

The impedance Z_t which will vary with excitation frequency ω can be found as

$$Z = V_{AC}/I_{AC} \qquad \text{(eq. 2.3)}$$

Using Euler's relationship, Z_t can be written as a complex number.

$$Z_t = Z_o\,[\cos(\varphi) + i\sin(\varphi)] = Z_{Re} + Z_{Im} \qquad \text{(eq. 2.4)}$$

With the impedance split into real and imaginary parts, it can be readily displayed on a Nyquist plot as shown in Figure 2.13. The magnitude of the total impedance $|Z|$ can be found by drawing a line straight from the origin to any point on the curve where the angle between this line and the real axis is the phase shift. The high frequency signals start at low real impedance values and get smaller as the real impedance increases. The intercepts with the real axis show the bulk resistance, R_{bulk} which consists of ionic resistance of electrolyte and electronic resistance of the electrodes, current collectors, and leads. The polarization resistance, R_p includes overpotentials associated with the chemical process in both the cathode and anode.

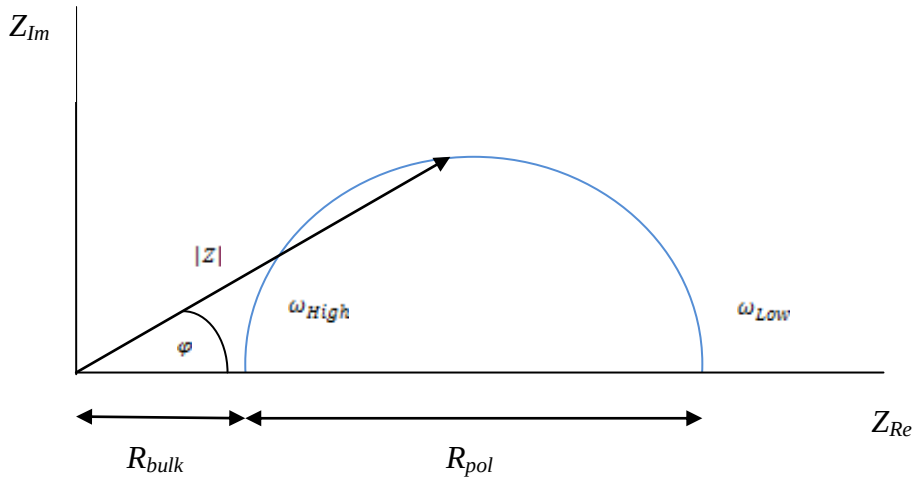

Figure 2.13 EIS curve in blue with absolute impedance $|Z|$ and angle φ. Bulk, R_{bulk}, and polarization resistance, R_{pol}, are at the real axis intercepts with the high and low frequencies, respectively.

2.3.4. Stability Testing

In order to obtain the performance of the button cells over a significant period of time, stability tests were run for as long as 48 hours. After the cells were conditioned, they were tested for stability under no humidity (baseline case), changes in fuel/oxidant depletion tests (FD and OD), and then for stability in humidified environments. Anode humidity and cathode humidity tests (AH and CH) were run following the FD and OD tests as they were the only tests known to permanently damage the cell. For stability testing, baseline cases were run for 48 hours to give a time period (longer than a UUV target mission) long enough to show degradation of cell performance. The fuel and oxidant depletion tests were

not stability tests, but the cells remained at these conditions for > 3 hours to ensure a steady state before LSV and EIS tests were run. This was sufficient enough since there was no change in performance other than what the baseline cases would show. It would have been ideal to run longer test periods under FD and OD to rule out any possible degradations of performance attributed to depletion. Humidity tests were run for 24 hours, followed by a dry test to investigate a chance of passivation as seen in literature for Ni/YSZ/LSM cells [20].

The objective of stability testing was to get the ideal operating conditions for a UUV SOFC power system with air-independent energy dense fuel and oxidant (Al oxidation and H_2O_2 decomposition). With humidified fuel and oxidant streams at high concentrations (> 20 mol% H_2O), an actual fuel cell would experience even higher concentrations down the channel. Here, we will show the performance of LT SOFCs under 20-50 mol% H_2O. Initial studies have shown that while under humid conditions on an LSM cathode, cell operating current densities (0.25-0.75 A/cm^2) could have an effect on the stability of an SOFC's performance [30], especially at lower temperatures. In the present study, it is of utmost importance to know the level of humidity that LT SOFC materials can tolerate, while at an operational voltage ideal for a UUV SOFC.

Chapter 3: Experimental Results and Discussion

3.1. Baseline SOFC Button Cell Test

SOFC cells were fabricated and conditioned, as discussed in Chapter 2, and then run at various baseline conditions to compare their performance. Tests included voltammetry, EIS, and *V-i* curves for cell stability. Table 3.1 shows the operating conditions for the voltammetry tests. Two different current densities were explored so as to subtract out any voltage decrease that may occur from the baseline in humidity tests. Decreases in voltage over time, more likely due to button cell cracks increasing in size, would be removed from fuel/oxidant humidity tests to focus on the changes occurring due to the varying operating conditions.

Table 3.1 Operating conditions for running a baseline test to compare cells.

Temp (°C)	**Anode Flow H_2/Ar**	**Cathode Flow O_2/N_2**	**Anode Humidity mol%**	**Cathode Humidity mol%**	**Current Density (A/cm^2)**
600, 650	48.4% / 48.4%	21% / 79%	3	0	0.17, 0.3

The results from baseline tests at 600 and 650°C without any cathode humidity for over a 24-hour period did not indicate any degradation of cell performance. The decline in voltage was no more than 0.1 mV in 24 hours at both current densities. *V-i* and EIS tests before and after the baseline voltammetry tests show only small variations in the *V-i* curves up to 0.8 A/cm^2.

After the baseline tests, cells were tested under different parameters to simulate conditions a SOFC may experience with fuel and oxidant for a UUV

application, as discussed in Chapter 1. To this end, tests at varying partial pressures of fuel and oxidant provided data on the performance with varying degrees of fuel and/or oxidant depletion. These conditions simulated various locations along the length of the anode and/or cathode channels for a full SOFC stack. The range of conditions tested provide a basis for validating stack models that need to simulate a wide array of conditions as the fuel and/or oxidant are depleted along the channel.

In addition to reactant depletion, tests were conducted with excess humidity in the cathode flow to simulate the potential oxidizer composition created from the decomposition of H_2O_2 as discussed in Chapter 1. Cells were tested for up to 1 month depending on whether significant degradation occurred in the cell, due to cathode exposed to high humidity. All experimental tests were run between 550 and 650°C while altering gas flows, the amounts of water in the flow, and the current density. Discussions on the test results in the following sections are split into respective anode and cathode flow condition sections.

3.2. Impact of Anode Flow Conditions

Two different types of anode flow tests, fuel depletion tests (FD) and anode humidity tests (AH), were performed as listed in Table 3.2. For FD tests, H_2 was depleted by increasing the Ar mol% while keeping the humidity at 3 mol% H_2O and the H_2 flow rate constant. In AH tests, the H_2 and Ar flow rates were kept constant while the bubbler temperature for humidification was increased (to 60 and 76°C) to reflect 20 and 40 mol% H_2O. The cathode oxidant

flows stayed constant with an air flow rate of 315 sccm and no humidity throughout all of these anode fuel flow tests.

Table 3.2 List of experiments performed, focusing on changes to anode fuel composition with constant dry air conditions at the cathode.

State	Type of Test	Temp (°C)	Anode Flow H_2/Ar	Cathode Flow O_2/N_2	Anode Humidity (mol%)	Current Density (A/cm^2)
1	FD	600 550	30%/67%	21%/79%	3	*V*-*i*/EIS
2	FD	600 550	20%/77%	21%/79%	3	*V*-*i*/EIS
3	FD	600 550	15%/82%	21%/79%	3	*V*-*i*/EIS
4	FD	600 550	10%/87%	21%/79%	3	*V*-*i*/EIS
5	AH	600 550	50%/30%	21%/79%	20	0.3
6	AH	600 550	50%/10%	21%/79%	40	0.3

3.2.1. Anode Fuel Depletion

Results for states 1 – 4 at 600°C in Table 3.2 included fuel depletion tests that varied the H_2 fuel content from 10 to 30 mol%. Figures 3.1 - 3.3 show the results. For all these figures the legends are the same, seen in Table 3.3, where the conditions are paired with a respective shape that is the same for both the *V*-*i* and EIS tests (grey filled for power density curves).

Table 3.3 Anode Depletion Conditions Legend

Test/State	% H_2	% Ar	$P_{O2,eff}$ (bar)
Base Case	48	48	5.0e-27
FD/1	30	67	1.6e-26
FD/2	20	77	3.6e-26
FD/3	15	82	6.5e-26
FD/4	10	87	1.4e-25

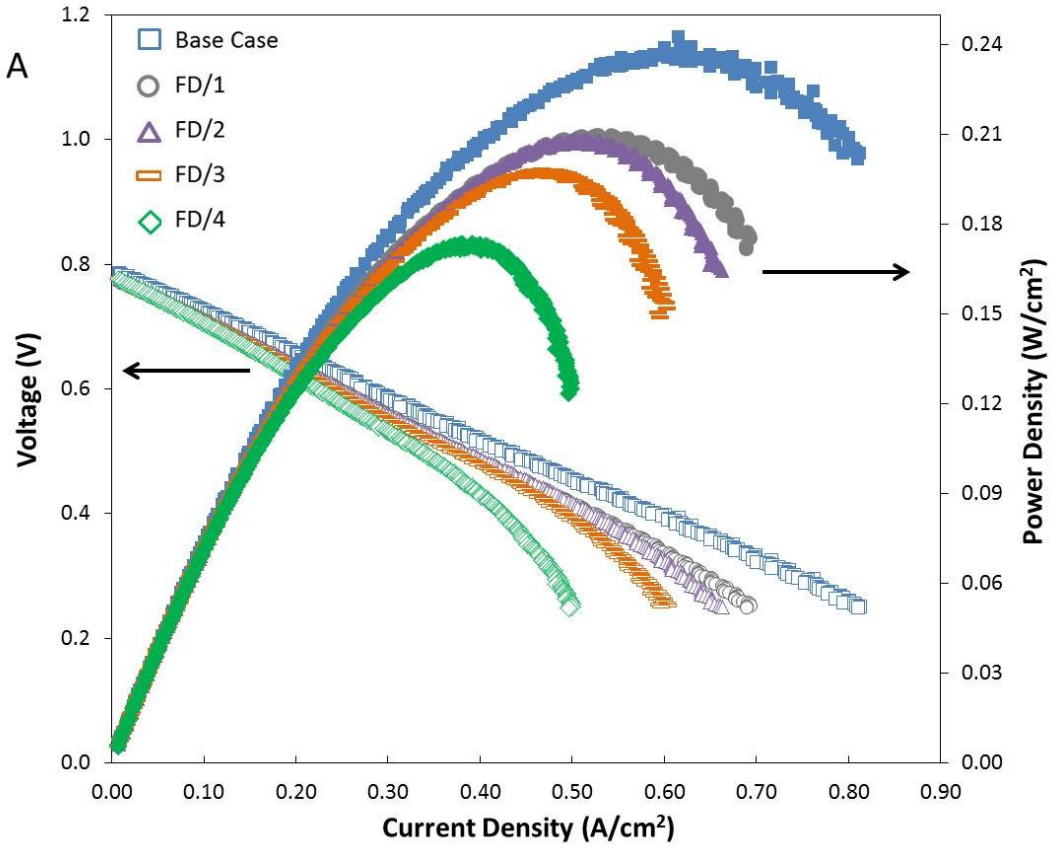

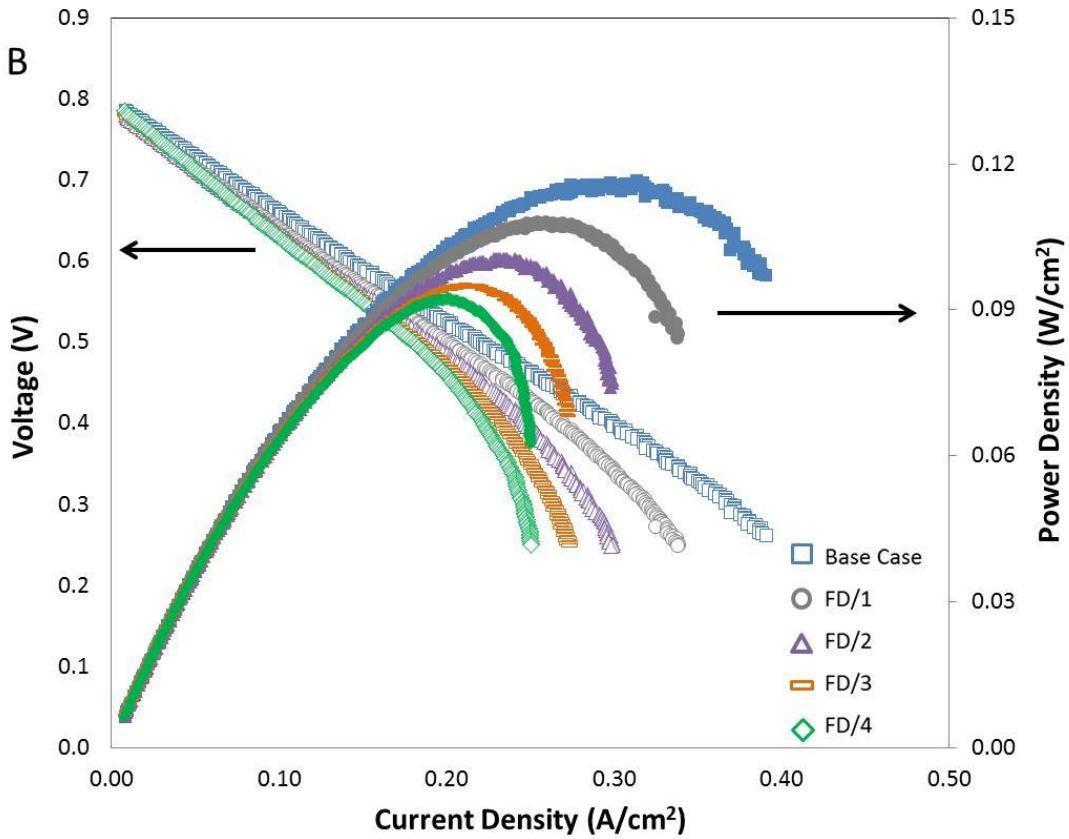

Figure 3.1 *V-i* curves showing the H_2 depletion tests at the anode at A.) 600°C and at B.) 550°C while running constant dry air conditions at the cathode.

In Figure 3.1 A and B, the ASR is of particular interest in the FD tests at voltages above 0.6 V/cell where most SOFCs will likely operate due to efficiency concerns. For lower voltages particularly at lower H_2 partial pressures overpotentials likely due to mass transport limitations become apparent causing ASR to increase significantly with current density from its low-current (high voltage) value. At 550°C, in Figure 3.1 B, similar results are seen, although the ASR becomes larger at the higher end of the *V-i* curve around 0.15 A/cm^2 (0.65 V). A comparison of H_2 depletion has been seen in work done by Chen et al. for

cathode supported cells with Ni/GDC anodes [42]. They operated their cells at 0.32 A/cm^2 at 800°C under 7.4% H_2 diluted in Ar and showed that the higher current density caused the cell voltage to degrade over time with the depletion of H_2. The steady decrease in voltage was more than likely associated with the buildup of NiO. At such high temperatures, the increased electronic conductivity of the GDC membrane causes higher fluxes of O^{2-} ions and increased P_{O2} in the anode, which encourages Ni oxidation.

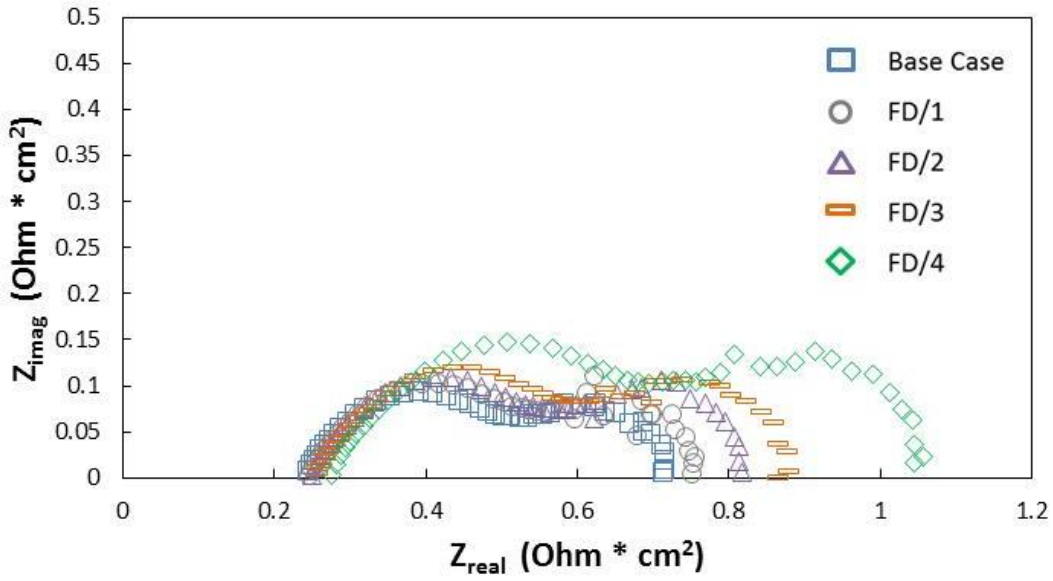

Figure 3.2 EIS tests at 600°C run at 0.3 A/cm^2 for the same FD tests, listed in Table 3.3, with dry air at the cathode.

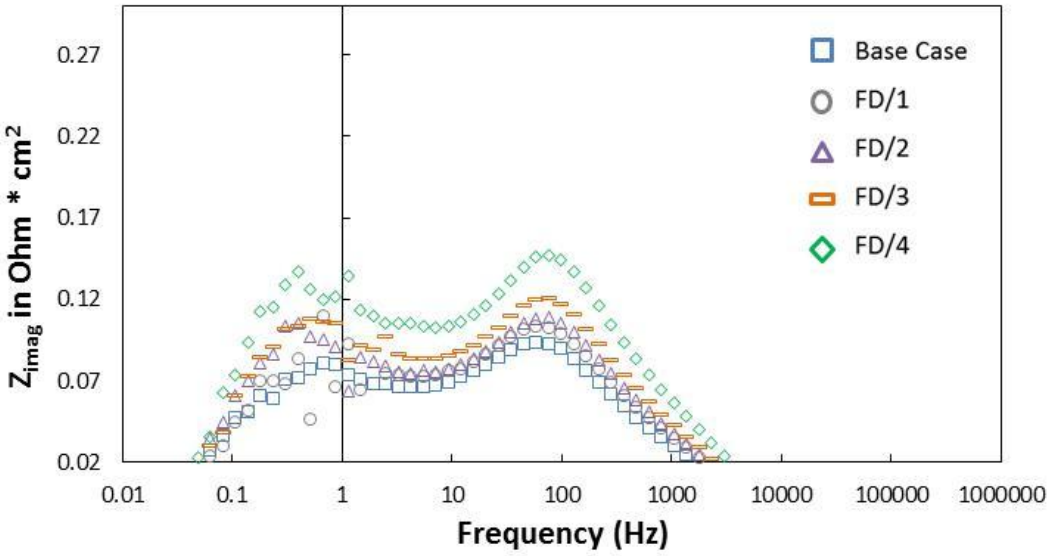

Figure 3.3 The imaginary impedance versus frequency of the same data shown in Figure 3.2, to compare characteristic frequencies over the operating conditions for the Base Case and states 1-4.

The Nyquist plot for EIS tests in Figure 3.2 for the base case and states 1 – 4 at 600°C and 300 mA/cm^2 illustrate how the H_2 depletion impacts polarization resistance (R_{pol}) at higher current densities. Unlike at lower overpotentials where R_{pol} is not significantly impacted by H_2 depletion, the higher current densities lead to increases in both the low and high frequency arcs. As H_2 mole fractions drop below 20%, the high frequency arc increases in magnitude while not changing characteristic frequency, suggesting perhaps a loss in electrocatalyst surface utilization at the lower H_2 concentrations. This could be implying nickel oxidation covering the electrocatalyst surface. The low frequency arcs changes more dramatically with more H_2 depletion. Changes in R_{pol} due to mass transport

limitations likely occur at the lower frequencies <10 Hz, as illustrated by the low frequency arc with characteristic frequencies of 0.8 Hz in Figure 3.3.

In the case of a full SOFC stack, the concentration of H_2 down the length of the channel decreases, therefore creating locations of H_2 depletion. The results in FD tests provide evidence that operating at higher voltages (> 0.6 V) will not only provide a higher efficiency, the cell performance will not be compromised by H_2 depletion down to 15%, at least for short periods of time. Further investigation of fuel depletion on long-term operation at high voltage is needed to ensure SOFC performance without degradation.

3.2.2. Anode Humidity Conditions

Button cells were tested under anode humidity (AH) to simulate an aluminum oxidation reactor exhaust. Holzer et al., [25] reviewed the impact of dry and humid atmospheres at 950°C on nickel grain growth, a thermodynamically driven process resulting in anode microstructure degradation. In their study, YSZ electrolyte-supported symmetric cells were tested with different compositions of the anode layer (Ni/GDC in weight ratios of 70:30 and 50:50). While operating at 60 mol% H_2O atmospheres, the percentage of grain growth in the first 100 hours for the 70:30 composition was double the growth with the 50:50 composition. In both cases, the humid atmosphere caused an initial increase in grain growth which plateaued after 200 hours of exposure. This plateau was a result of a continuous GDC layer formation on the nickel, which

prevented further grain growth. Dry atmospheres (3 mol% H_2O) showed less than 3% grain growth after 2000 hours.

For the current study, measurements were taken at a lower temperature 650°C more characteristic of expected operating conditions for GDC electrolyte cells. The lower temperatures reduce losses due to GDC electronic conductivity at the higher temperatures and low P_{O2eff} associated with the anode. This electron conductivity arises from reduction of the ceria (Ce^{4+} to Ce^{3+}) in the GDC under reduced conditions. The reduction can result in expansion of the lattice that can cause structural damage to the anode [43].

The testing parameters for AH tests are in Table 3.2, states 5 and 6. Operating at 20 mol% H_2O at 0.3 A/cm^2 showed a negligible decline in voltage, 0.04 mV/hr (after base case voltage degradation was removed), for a 24 hour period. At 40 mol% H_2O and the same current density, the decline in voltage was 0.2 mV/hr (after base case voltage degradation was removed) for a 24 hour period. *V-i* measurements taken at 20 and 40 mol% H_2O tests are displayed in Figure 3.4. The legend also shows how P_{O2eff} increases with H_2O mole fraction. No clear change in performance is seen at current densities below 0.4 A/cm^2, suggesting that the increase in P_{O2} due to H_2O content does not impact the surface chemistry. Rather only H_2O mass transport limitations away from the functional layer at high current densities impact R_{pol} at least for the first 24 hours of cell operation.

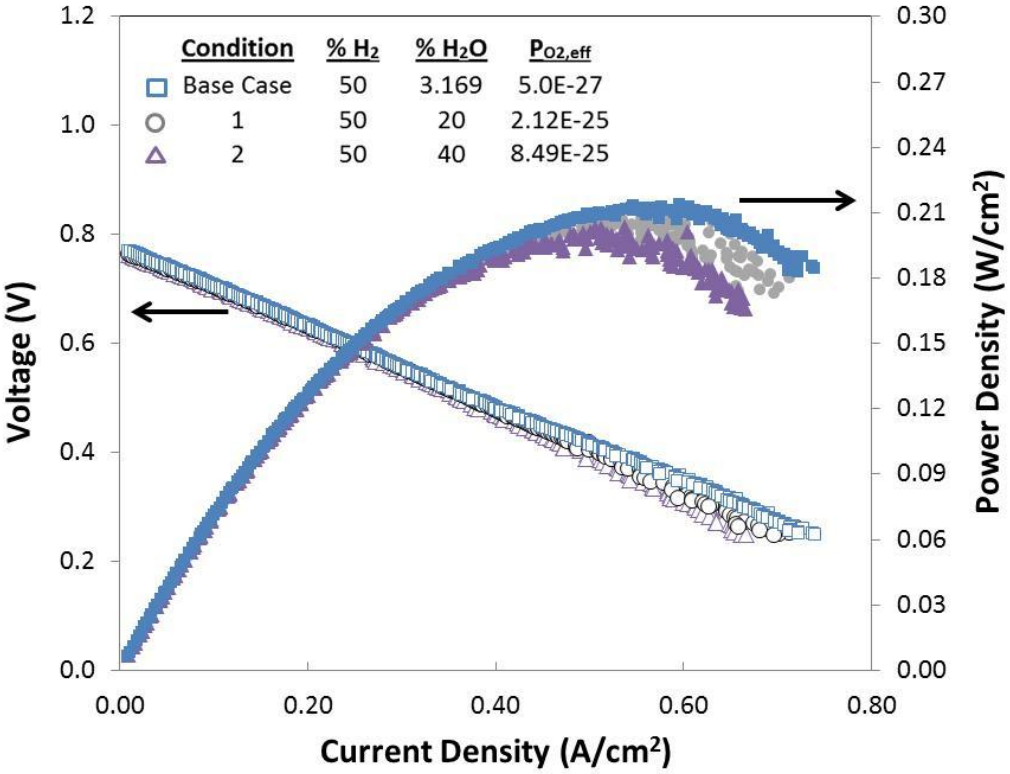

Figure 3.4 *V-i* curve of button cell operating at 600°C under 3, 20, and 40 mol% H_2O.

With results from anode depletion and humidity testing, conclusions can be drawn for determining the best operating conditions for a SOFC using air-independent, energy dense fuels like Al oxidation in water for a UUV. With varying H_2 partial pressure down the channel of a SOFC, minimal changes in performance should be seen while operating at high voltages (> 0.6 V/cell) and reasonable H_2 mole fractions down to at least 15 mol%. For the humidity tests, operating at lower temperatures with anode humidity below 40% at 0.3 A/cm^2 seem promising for a UUV utilizing energy dense aluminum fuel for a SOFC. No clear indication of nickel grain growth was present for the time scales of the

current tests, but further investigation of long term anode humidity tests are needed to assess this more conclusively.

3.3. Impact of Cathode Flow Conditions

For an air-independent UUV, H_2O_2 decomposition to provide O_2 for a fuel cell cathode can present unique challenges with respect to humidity levels inside the cathode flow channel.

Table 3.4 Tests reviewing the effects of oxygen depletion (OD) and cathode humidity (CH) on the performance of the cell.

State	Type of Test	Temp (°C)	Anode Flow H_2/Ar	Cathode Flow O_2/N_2	Anode Humidity (mol%)	Cathode Humidity (mol%)	Current Density (A/cm^2)
1	OD	650 600 550	48.5%/48.5%	21%/79%	3	0	*V-i*/EIS
2	OD	650 600 550	48.5%/48.5%	18%/82%	3	0	*V-i* /EIS
3	OD	650 600 550	48.5%/48.5%	13%/87%	3	0	*V-i* /EIS
4	OD	650 600 550	48.5%/48.5%	8%/92%	3	0	*V-i* /EIS
5	OD	650 600 550	48.5%/48.5%	5%/95%	3	0	*V-i* /EIS
6	CH	650	48.5%/48.5%	16.8%/ 63.25%	3	20	0.17
7	CH	650	48.5%/48.5%	10.5%/ 39.5%	3	50	0.17
8	CH	650	48.5%/48.5%	10.5%/ 39.5%	3	50	0.34
9	CH	650	48.5%/48.5%	21%/79%	3	0	0.34

To explore the effects of cathode humidity on GDC based SOFCs for UUV applications, button cell SOFC tests were performed on a range of cathode gas

composition exploring oxygen depletion (OD) tests as well as cathode humidity (CH). For these tests the anode gas flow rates were constant under 48.5 mol% H_2, 48.5 mol% Ar, and 3% H_2O. Table 3.4 lists the two different types of tests performed focusing on cathode gas composition variation.

3.3.1. Cathode Oxygen Depletion

The OD tests were run by increasing the N_2 mol% while keeping the total volumetric flow rate constant. Five different compositions were explored (States 1 - 5 in Table 3.4) using pure air as the maximum oxygen concentration. Figure 3.5 shows the impedance graphs of condition 1 at temperatures 550, 600, and 650°C. At 600 and 650°C the two usual peaks observed in previous tests for these cells is seen, but when the case for 550°C is run, there is a stray from the two peaks to include what appears to be one or two additional peaks. The polarization resistance also increases significantly between each temperature.

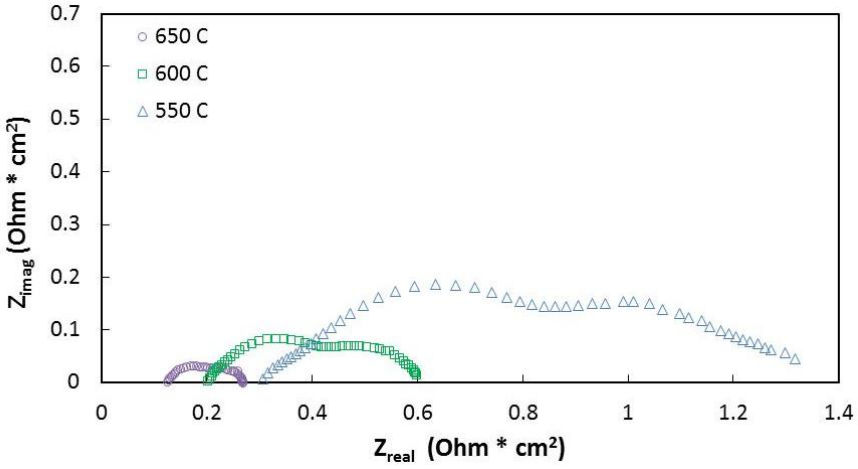

Figure 3.5 EIS tests run at three temperatures at the same oxygen partial pressure of 0.21 bar.

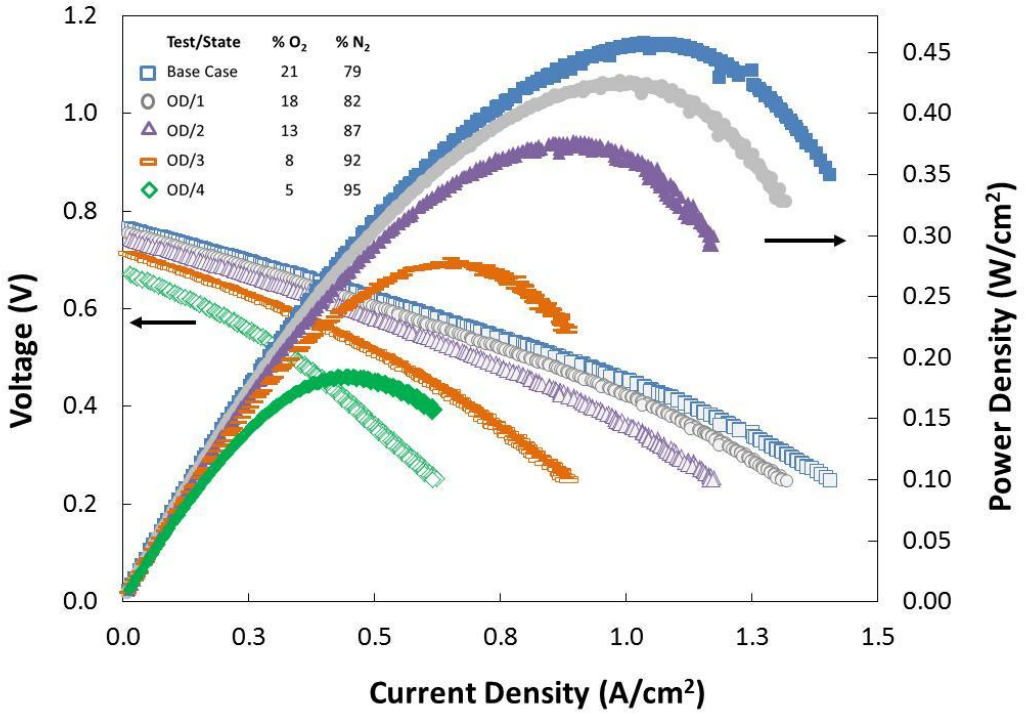

Figure 3.6 *V-i* curves at 650°C operating at PO_2 from 0.5 to 0.21 bar at cathode.

V-i curves for states 1 - 5 at 650°C were taken to investigate oxygen partial pressure reduction at the cathode and its effect after running 1 - 2 hours. These plots can be seen in Figure 3.6. The *V-i* curves contain evidence of mass transport in addition to lowering of OCV with decreasing P_{O2}. The lowering of OCV can be associated with a reduction of the GDC, promoting a more amenable situation for electronic conduction as the ceria in the GDC reduces from Ce^{4+} to Ce^{3+}. The OCV and ASR (taken between OCV and 0.6 V) with P_{O2} at the cathode at 650°C, 600°C and 550°C is displayed in Figure 3.7. The decrease in OCV with increasing temperature is normal for doped ceria electrolytes due to the MIEC quality, although the partial pressure of oxygen plays an important role in maintaining the

OCV as well. The OCV in combination with the ASR contribute to the overall power density through equation 3.1.

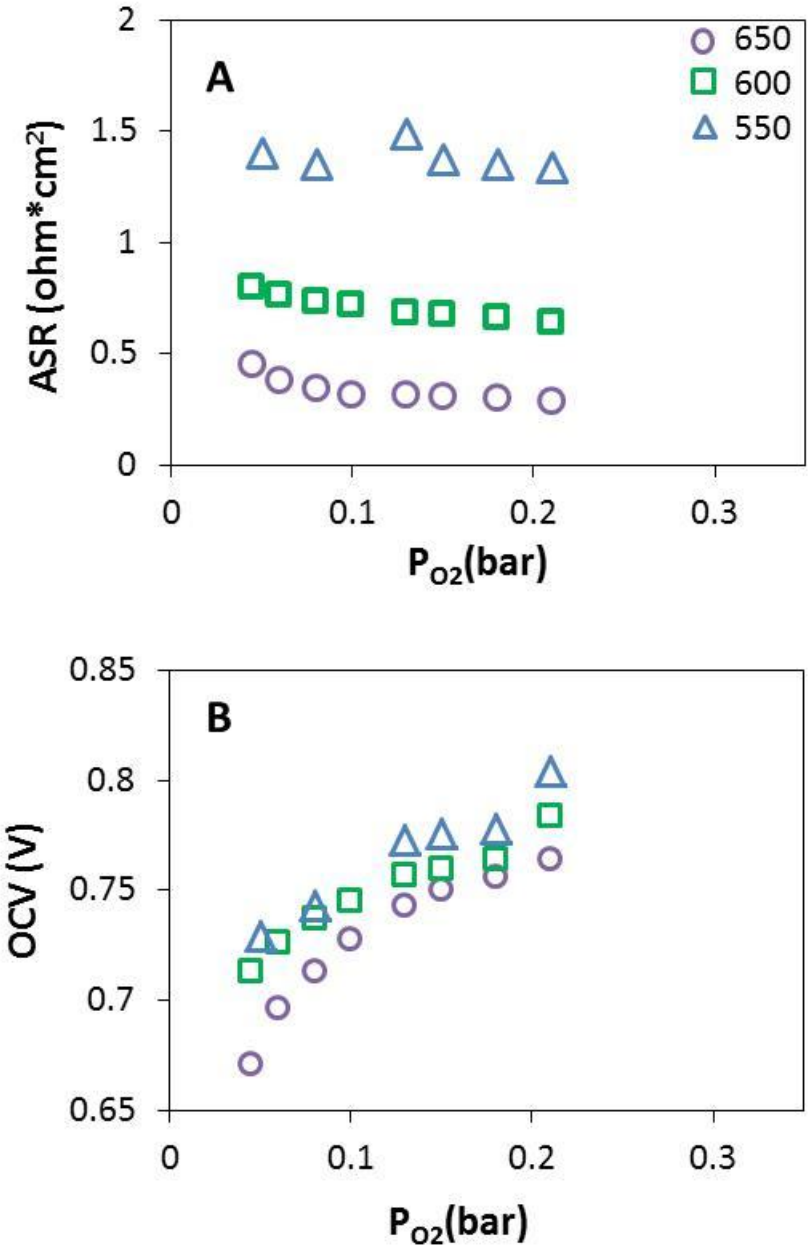

Figure 3.7 A.) ASR and B.) OCV values at various P_{O2} at 650°C, 600°C, and 550°C.

$$\dot{W}_{\text{elec}} = V_{cell} \times \left(\frac{OCV - V_{cell}}{ASR}\right) \qquad \text{(eq. 3.1)}$$

3.3.2. Cathode Humidity Conditions

The results from humidity tests at the cathode revealed an interesting relationship between operating potential and cell performance. Conditions 6 - 9 in Table 3.4 represent low and high humidity tests at 20 and 50 mol% water at a low current density, 0.17 A/cm^2. Operating at 650°C revealed a small change in performance for both humidity cases, shown in Figure 3.8. A change from 20 to 50 mol% H_2O does not change the voltage at 0.17 A/cm^2 by more than 40 mV. A slight increase in voltage has been seen in another related work by Kim et al. [21] on LSM cathodes with ScSZ (scandium stabilized zirconia) electrolytes at low amounts of humidity (< 4% H_2O in air). Tests of up to 40% H_2O found a decrease (or step down) in voltage over a period of 5 hours. Longer testing would be needed to show if there was a gradual degradation, similar to that shown in the previously mentioned work with YSZ/LSM cells by Nielsen et al. [20].

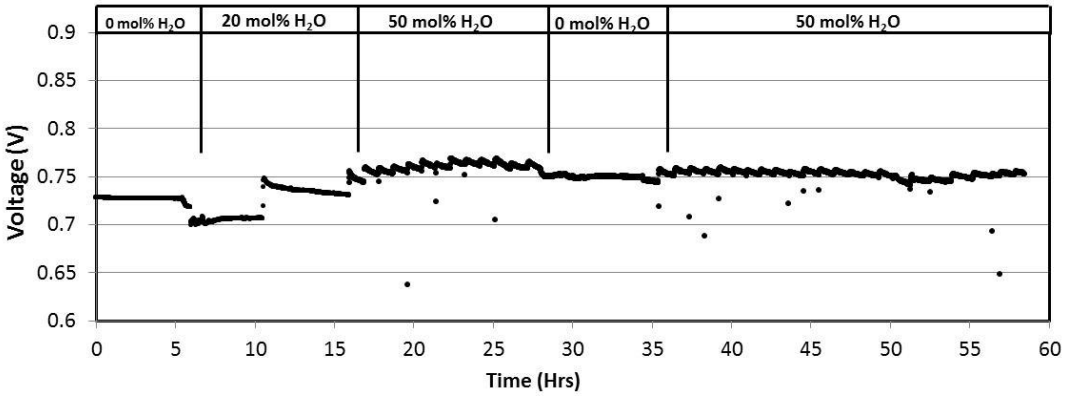

Figure 3.8. Volammetry of button cell operation at 650°C under 0.17 A/cm^2 at 0, 20, and 50 mol% water. Slight improvements of 40 mV are seen when humidity is applied at this lower current density.

In the work of Sakai et al. [44], an increase in the interfacial conductivity of 30% for a short period of time (< 2 min) under < 2 mol% H_2O on gold electrodes with YSZ electrolytes at about 600°C was observed while the bulk conductivity of the same samples stayed constant. After those 2 minutes, however, the interfacial conductivity degraded and was not recoverable even after dry air was run. An explanation of the increase in interfacial conductivity, proposed by Sakai et al., is the electrocatalytic effect of water expanding the active area and tpb where water could be a part of a charge transfer reaction:

$H_2O_{ad} \Leftrightarrow H_2O_{gas}$ (Reaction 3.1)

$H_2O_{ad} + O_{ad} + 2e^-$ (from electrode) $\Leftrightarrow 2OH^-_{ad}$ (Reaction 3.2)

$2OH^-_{ad} \Leftrightarrow O^{2-}$ (in YSZ) + H_2O_{ad} (Reaction 3.3)

In reaction 3.1 and 3.2, H_2O adsorbs and then dissociates on the surface of the electrode and combine with electrons to form surface hydroxyls, which readily take on electrons from the electrode to form OH^-. In reaction 3.3 OH^- ions dissociate and form an O^{2-} ion and water where the water would move from the surface to the gas phase. This reaction suggests that H_2O can serve as a mechanism for accelerating O^{2-} formation in the cathodes.

It should be noted that Sakai et al. [44] tested GDC electrolytes with gold electrodes and found very different results due to possible exposure to humid elements during fabrication. Questions remain about the impact of H_2O and O_2 reduction in GDC/LSCF cathodes.

The results of higher current density (0.34 A/cm^2) tests with humidity at the cathode showed degradation at 50 mol% H_2O. Figure 3.9 reveals the voltage degradation over 72 hours at these conditions. When dry air was run afterwards, the voltage was not recoverable and irreversible damage to the cell was evident. The circled numbers within the graph in Figure 3.9 represent points at which EIS tests were run to see how the impedance changed with humidity and time, seen in Figure 3.10 and 3.11. The baseline voltage degradation, 0.1 mV/hr, was removed from the humid cathode voltage degradation measurements, resulting in 0.8 mV/hr voltage decline between points 1 and 2 in Figure 3.9, a higher degradation of 1.6 mV/hr between point 2 and 3, and the largest degradation of 3.7 mV/hr between points 3 and 4.

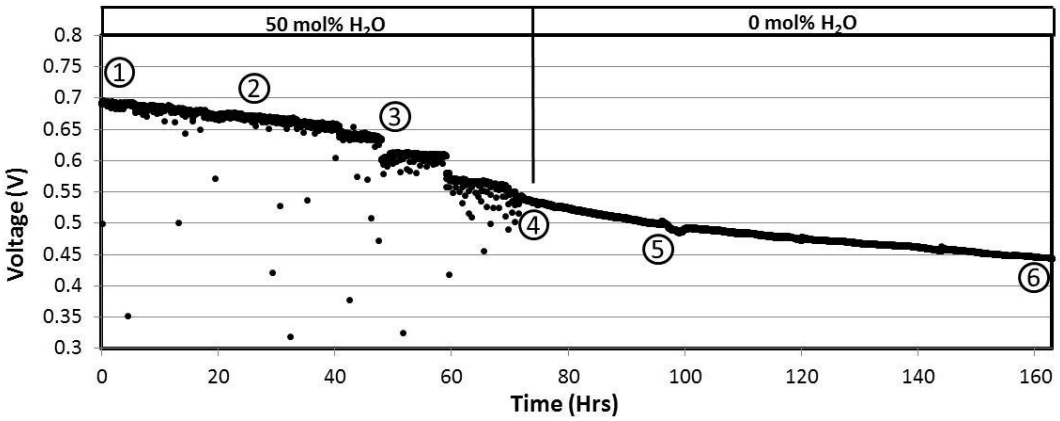

Figure 3.9 Volammetry of button cell operation at 650°C under 0.34 A/cm^2 at 50 mol% H_2O for 72 hours. Cell degradation and irreversible damage to the cell is evident after dry air was run for 90 hours.

The shape of the impedance curves in Figure 3.11 change over the course of this test. At point 1, before humidity was applied to the cathode, the lower frequency peak had slightly higher impedance than the high frequency peak. As

the cell sat at 50 mol% water for over 24 hours, point 2, the high frequency peak started to grow as well as the polarization and bulk resistance up until the 72 hour mark, point 4. When dry air was run after this humidity test, point 5 and 6, the bulk resistance stopped growing and there was a shift back to the shape of the dry air condition impedance with a lower high frequency peak and a high low frequency peak. This transition is more easily seen in Figure 3.11 where the high frequency peak positions do not change with frequency, only the impedance changes. At lower frequencies it is difficult to make out the second peak for the humid cases. These transitions with 50 mol% humid air suggest a higher activation overpotential associated with the electrocatalytic active regions, and a lower mass transport overpotential associated with the diffusion of reactant (O_2 and now H_2O).

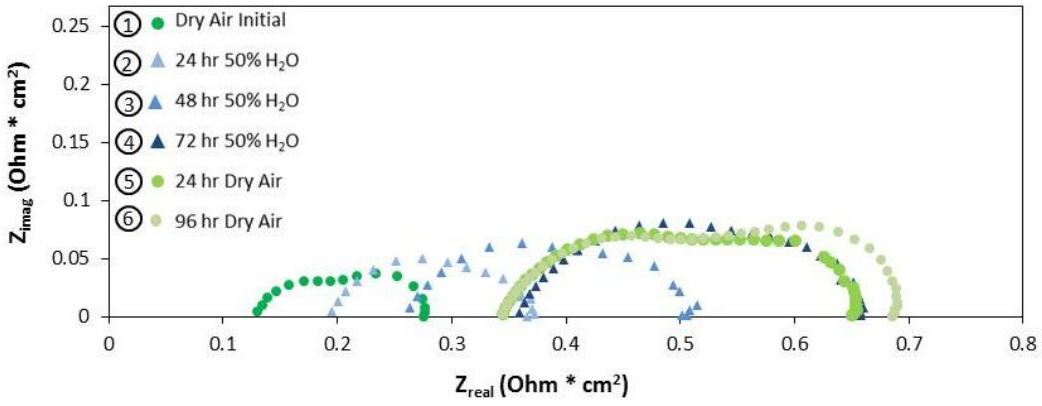

Figure 3.10 Comparison of EIS graphs at OCV at various points during testing. The circles represent dry air conditions while the triangles represent humid air conditions.

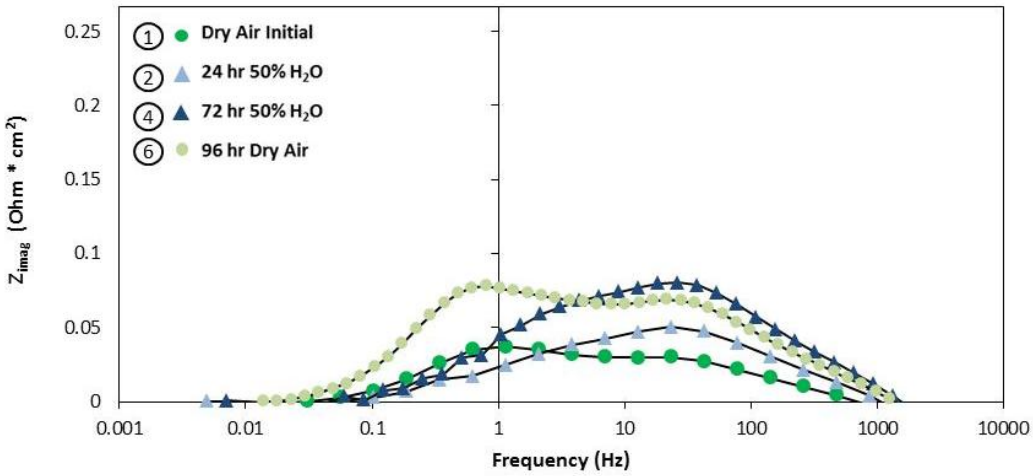

Figure 3.11 Imaginary impedance with frequency at four different points of the test shown in Figure 3.10, mixture of dry and humid conditions at 650°C.

Voltage degradation has been seen for LSM cathode and YSZ electrolyte pairs a <13mol% H_2O at 750°C [20, 45]. Hagen et al. also showed that degradation of LSM and YSZ cathodes in humid atmospheres was mitigated by increasing the operating temperature to 850°C and decreasing current density tend to mitigate the effect of humidity [30].

There have been limited studies on the effects of cathode H_2O mol% for LSCF/GDC cathodes. Bucher et al. studied LSCF O_2 exchange kinetics in humid atmospheres and found that 1% H_2O increased formation of surface strontium oxide, lanthanum oxide, and strontium-rich silicon layers, which lowered the O_2 surface exchange coefficient [46]. X-ray photoelectron spectroscopy (XPS) measurements from this study show depth profiles up to 400 nm and the existence of silicon poisoning 10 nm from the surface to the bulk of LSCF after a long exposure (about 1000 hours) to humid conditions. Dry cases of the same cells

showed no silicon poisoning, proof that the presence of water at the cathode can increase silicon poisoning if there is any silicon available in the vicinity (glass seals, insulation, etc.).

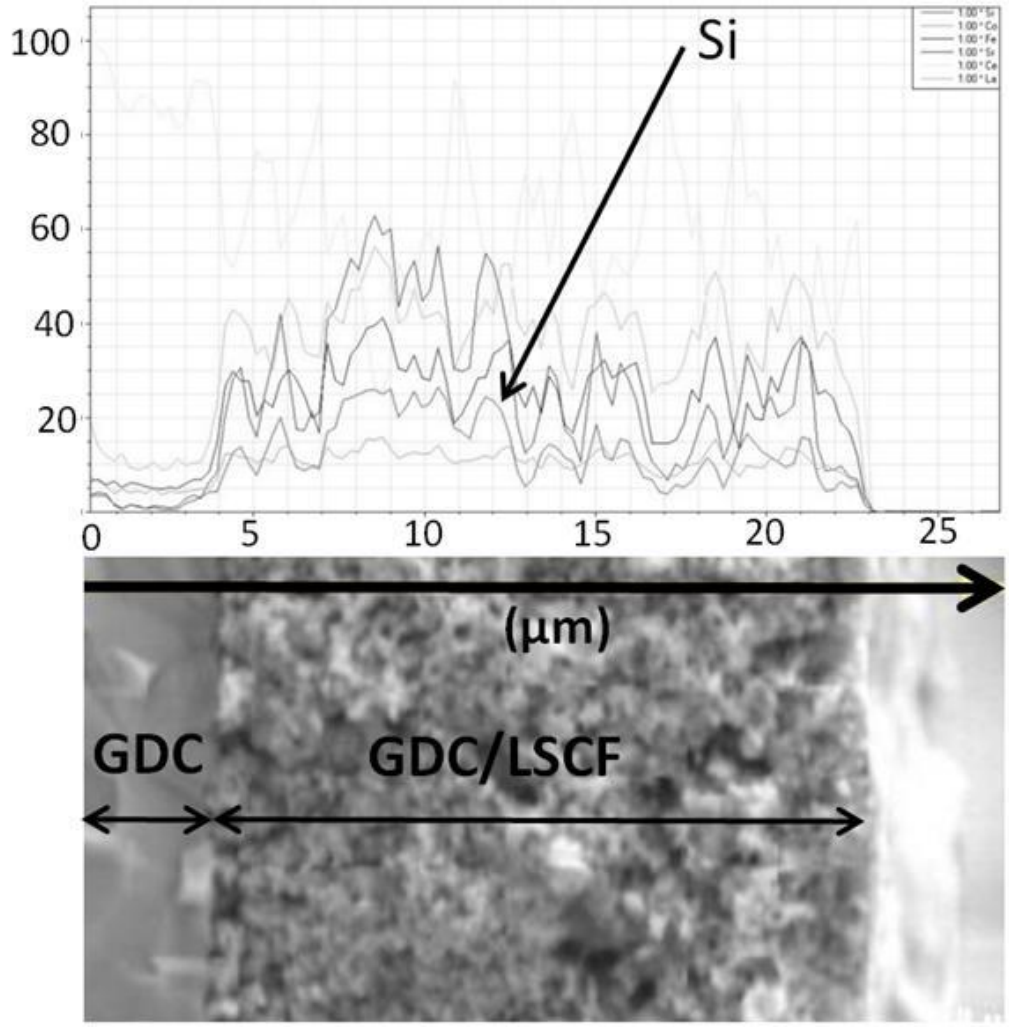

Figure 3.12 EDS of electrolyte/cathode cross-section of post-mortem cell tested at 20 and 50 mol% H_2O conditions at 650°C to investigate silicon poisoning.

It is quite difficult to avoid silicon contamination in SOFC testing due to commonly used glass seals and insulation. It is possible that the sample in the current study contained silicon impurities. Therefore, energy-dispersive x-ray spectroscopy (EDS) of a tested cathode was performed to see if silicon resided on

the surface of a post-mortem cell tested under 20 and 50 mol% H_2O conditions. The most silicon was found at about 15 μm down into the surface, seen in Figure 3.12. This signal strength was slightly greater than what was considered to be noise and thus it was inconclusive if Si was impacting cathode degradation observed in this study.

Cathode depletion and humidity experimental results revealed a few interesting trends. At a range of P_{O2} (0.05 - 0.21 bar), ASR does not significantly change for the anode-supported GDC cells tested in this study, although a shift in ASR is most certainly present, 0.3 to 1.5 Ω*cm^2, between 550 and 650°C. The effect of low P_{O2} atmospheres on OCV for these GDC cells shows a clear connection with increased electronic leakage (seen in low OCV values 0.66 V at 0.04 bar P_{O2} compared to 0.76 V at 0.21 bar P_{O2} at 650°C) due to ceria reduction. These findings are important parameters when deciding on the operating conditions in which to run a SOFC, particularly for a UUV application. For example a tradeoff between lower operating temperatures with quick start-up times opposed to having a lower ASR to achieve higher cell power densities with improved efficiencies at higher operating voltage. The reduction in P_{O2} simulates the idea of reduced availability of oxygen down the length of an SOFC channel. Knowing that the OCV is quite variable with P_{O2}, an extensive study of H_2O_2 decomposition reactor controls is needed for optimizing the OCV and resultant power density during operation.

Humidity test results were highly dependent on operating current densities for 20 and 50 mol% H_2O. Slight improvement in voltage, for 10-15

hours, occurred at 0.17 A/cm^2 for both 20 and 50 mol% H_2O. This could possibly be attributed to a an increase in interfacial conductivity caused by the production of OH^- ions, in turn producing O^{2-} ions available at the electrolyte/cathode interface. However, at current density 0.34 A/cm ^{2}, the voltage degraded at a rate of about 3.8 mV/hr after 48 hours in 50 mol% H_2O and was irreversible after flowing dry air for over 90 hours. Further investigation is needed for a wider range of operating temperatures and its effect on cell performance in humid atmospheres, as well as investigation of longer operating times at lower current densities.

A H_2O_2 decomposition reactor providing O_2 and heat, and H_2O for a SOFC cathode inlet may be plausible for a UUV system, depending on the operating voltage and the amount of water that may be removed from the cathode inlet. Lowering the H_2O content from the O_2 supply via condensing the water in an intermediate heat exchanger before cathode inlet heating will provide a valuable approach to lowering the H_2O content to acceptable values. However, as O_2 depletion occurs along the anode, increases in H_2O mol% will occur, particularly for UUV applications where high cathode O_2 utilizations are preferred to optimize system energy densities. Chapter 4 will discuss some of these issues regarding SOFC operation and the trade-offs associated with O_2 utilization as well as cathode inlet preconditioning.

Chapter 4: SOFC System Analysis

4.1. UUV Power System

Translating the SOFC button cell performance into an assessment of UUV power system design and energy densities requires the development of an SOFC stack model not only for performance but also size. This chapter explores how the experimental button cell performance over a range of test conditions presented in Chapter 3 translates into an expected performance of a 2.5 kWe SOFC stack for an air-independent UUV power system. The SOFC stack performance and operating conditions provided the basis for specifying the balance of plant components for the UUV power system design and thereby calculating the resultant specific energy and energy density for a typical HWV Class UUV mission duration (20 - 100 hours).

For the proposed system illustrated by the schematic in Figure 4.1, decomposition of H_2O_2 in solution provides humidified O_2 for the SOFC cathode, and Al oxidation with recycled H_2O provided humidified H_2 for the SOFC anode. The compositions and flow rates from the upstream reactors – H_2O_2 decomposition for cathode O_2 and Al oxidation with H_2O for anode H_2 – require heat exchangers for getting the inlet flows in appropriate ranges for the SOFC inlets. Calculations for necessary size of the upstream reactors and associated heat exchangers give an estimated volume and weight of all the SOFC power system components and the reactants (Al, H_2O, and H_2O_2) needed for storage to achieve a particular UUV mission.

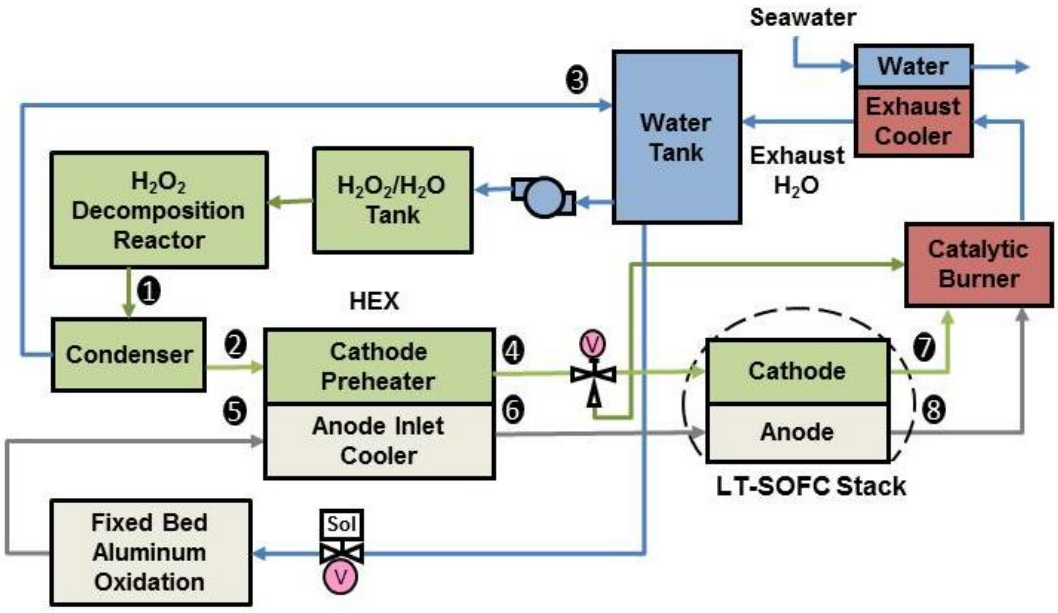

Figure 4.1 Schematic of proposed Al/H_2O_2 system design incorporating an exhaust cooler downstream of the aluminum oxidation reactor, a condenser downstream the H_2O_2 decomposition reactor, and heat exchanger between the cathode and anode inlet gases prior to entering the SOFC stack. After the SOFC, a catalytic burner is used to provide additional exhaust water to the storage tank. Seawater is used to provide cooling and a continuous recycled water stream provides water to the aluminum oxidation reactor.

The UUV power system design, in Figure 4.1, utilizes the large amounts of heat given off by the Al oxidation reaction. As discussed in Chapter 1, exothermic Al oxidation by H_2O (Reaction 1.5) with Δh_{reac} = -15.1 MJ/kg_{Al}, will likely produce steam and H_2 at the exhaust. The decomposition of H_2O_2, also exothermic with Δh_{reac} = -5.6 MJ/$kg_{H2O2\ Mix}$, will produce a mixture of O_2 and H_2O gases and liquid H_2O. Species and energy balances were made to determine the need for additional system components for condensing out H_2O or exchanging heat between gas lines. The following section reviews the calculations within the

model and the assumptions and simplifications behind them. The methodology for translating experimental button cell results to a simple stack sizing model is also discussed.

4.1.1 Assumptions and Methodology

Calculations for this study include modeling of the SOFC using experimental values to estimate operating voltages per cell and current density for the stack. The stack power density and anode fuel and cathode O_2 utilization (U_{H2} and U_{O2} respectively) provide the primary criteria for sizing the fuel and oxidizer reactors and associated heat exchangers to condition the SOFC reactants. Heat exchangers either between two flows or between available seawater and a flow are used to set gas flow temperatures desirable for the SOFC anode and cathode inlets. Component weight and volume and amount of reactants (Al, H_2O, and H_2O_2) needed for UUV missions between 20 and 100 hours were calculated to estimate the specific energy and energy density of the system as a function of mission duration and SOFC operating conditions.

SOFC inlet temperatures are set by having the feed streams for the cathode and the anode exchange heat with each other and reach thermal equilibrium. The very hot anode feed from the exothermic Al oxidation exhaust provides heat for the relatively cool humidified O_2 cathode feed leaving the condenser downstream of the H_2O_2 decomposition reactor. The required molar flow rates into the SOFC (determined from gross power demand and H_2 fuel and O_2 utilizations) provide

the basis for the Al/H_2O reactor and cathode feed condenser flows. These flows combined with simple zero-dimensional heat loss models for the two reactors are used to calculate the feed temperatures into the final heat exchanger upstream of the SOFC. The SOFC and Al/H_2O reactor contained heat loss *UA* values (2.2 and 12 W/K, respectively) that are reasonable based on standard heat transfer calculations.

The SOFC uses open circuit voltage (OCV) and area specific resistance (ASR) values taken from experimental results at 650°C to determine the average current density, i (A/cm^2). The data taken from experimental button cell tests is used to fit OCV and ASR values for the stack model. The OCV is primarily a function of temperature, P_{O2} at the cathode, and P_{H2} at the anode. The fitting does not include the variation of P_{H2O}, although when more button cell tests are conducted using humid atmospheres at both the anode and cathode, the results can be included in another fit for the OCV and ASR values.

A nonlinear least squares fitting tool was used to determine the calculated OCV value, OCV_{calc} with equation 4.1.

$$OCV_{calc} = 0.4 - 0.398\left(\frac{T}{T^0}\right) + 0.753\left(\frac{P_{O2,cathode}}{P^0{}_{O2,cathode}}\right)^{0.053}$$

$$+ 1.5E^{-4}\left(\frac{P_{H2,anode}}{P^0{}_{H2,anode}}\right)^{-1.999} \qquad \text{(eq. 4.1)}$$

Where T is operating temperature, T^0 is 923.15 K, $P^0_{O2cathode}$ is 0.21 bar, and $P^0_{H2anode}$ is 0.5 bar. The fitting tool compares the OCV_{calc} to the measured OCV values, OCV_{meas}, at various $P_{O2,cathode}$ and $P_{H2,anode}$. The standard deviation of the OCV_{calc} from the OCV_{meas} for this fit is 0.1.

The ASR is calculated for the SOFC stack similarly to the OCV fit. The calculated ASR, ASR_{calc} comes from equation 4.2 where it is also a function of temperature, $P_{O2,cathode}$, and $P_{H2,anode}$. Like OCV_{calc}, ASR_{calc} is not a function of P_{H2O} for this study.

$$ASR_{calc} = (7.96 \cdot 10^{-8}) e^{\left(\frac{1.29 \cdot 10^4}{T}\right)} + (1.497 \cdot 10^{-3}) e^{\left(\frac{573.14}{T}\right)} \left(\frac{P_{O2,cathode}}{P^0_{O2,cathode}}\right)^{-2.573}$$

$$+ (1.736 \cdot 10^{-7}) e^{\left(\frac{1.275 \cdot 10^4}{T}\right)} \left(\frac{P_{H2,anode}}{P^0_{H2,anode}}\right)^{-0.193} \qquad \text{(eq. 4.2)}$$

The standard deviation of the difference of ASR_{calc} and ASR_{meas} is 0.05, so the equation fits the data relatively well. Now that there is a functional relationship of OCV and ASR with temperature, P_{O2}, and P_{H2}, the current density and operating voltage can be calculated, given the power output desired.

A 10 x 10 cm^2 active area for each cell in the SOFC stack is assumed based on typical manufacturing constraints. The number of cells is determined from equation 4.3 where n_{cell} is the number of cells and A_{stack} is the sum of the active areas of all the cells.

$$\dot{W}_{stack,elec} = (V_{cell} n_{cell}) * (i A_{stack}) = V_{stack} * I_{stack} \qquad \text{(eq. 4.3)}$$

The electrical stack power, $\dot{W}_{stack,elec}$, is the combined net power, 2.5 kW, and parasitic power, 625 W, as seen in the parameters specified for baseline results in Table 4.1.

Table 4.1 List of SOFC baseline input values used to calculate composition and flow rate of species in and out of fuel cell and inlet temperature required. Grey cells are values taken from button cell experiments

Inputs to SOFC Stack	**Value**
Stack Outlet/Operating Temperature (K)	923.15
Net Power (W)	2500
Balance of Plant Efficiency	0.8
Parasitic Power (W)	625
Number of cells, n_{cell}	200
Active Area of cell, Ac_{ell} (cm^2)	100
Open Circuit Voltage (V/cell)	0.85
Area Specific Resistance (ohm*cm^2)	0.214
Average Voltage/cell (V)	0.81
Average Current Density (A/cm^2)	0.19
Average Power Density (W/cm^2)	0.16
Fuel U_{H2}	0.8
O_2 Stoichiometric Ratio	1.20
Anode H_2 Mole Fraction In	0.75
Anode H_2O Mole Fraction In	0.25
SOFC Stack *UA* (W/K)	2.2

With the calculated OCV and ASR and known power output there is a specified *V-i* curve that will provide a quadratic relationship to solve for *i* in equation 4.4. Equation 4.5 solves for the operating voltage, V_{cell}, using the current density solved for in the previous equation, *OCV*, and *ASR*.

$$(ASR)i^2 - (OCV)i - P = 0 \qquad \text{(eq. 4.4)}$$

$$V_{cell} = OCV - iASR \qquad \text{(eq. 4.5)}$$

Therefore, i and V_{cell} will change as n_{cell} and A_{cell} change.

From the current density, U_{H2}, O_2 stoichiometry, anode mole fractions of H_2 and H_2O (Table 4.1), and cathode inlet, O_2 and H_2O, (specified by the H_2O_2 decomposition reactor discussed later), the inlet flow rates for O_2 and H_2 are calculated from equation 4.6.

$$\dot{n}_{in,k} = \frac{i}{n_{elec}F}\,\lambda_k \qquad \text{(eq. 4.6)}$$

Here, $\dot{n}_{in,k}$ is the molar flow rate (mols/sec) into the electrode n_{elec} is the number of electrons transferred (depending on gas species: 2 for H_2 and 4 for O_2), F is Faraday's constant, and λ_k (= $1/U_k$) is the stoichiometric ratio of reactant k.

The energy balance in the fuel cell evaluates the power generated, enthalpy of inlet and outlet species and assumes a SOFC stack heat loss, variable by a *UA* value specified in Table 4.1. This *UA* value is adjusted to ensure the inlet temperature stays within the range of 500-815 K for SOFC stack operating temperature T_{out} = 923 K. Equation 4.7 describes the energy balance of the stack.

$$\sum h_{k,in}(T_{in})\,\dot{n}_{k,in} = \sum h_{\kappa,out}(T_{out})\,\dot{n}_{k,out} + \dot{W}_{elec} + \dot{Q}_{loss,stack} \qquad \text{(eq. 4.7)}$$

From input values in Table 4.1, $\dot{W}_{elec}$ is the sum of the net power from the stack:

3.13 kWe power out with 2.5 kWe net power + an estimated 20% of the net power

out (625 kWe) for balance of plant and power electronics needs. $\dot{Q}_{loss,stack}$ is the heat loss out of the stack based upon a *UA* of 3.5 W/K.

After solving for the mass flow rates and composition at the SOFC inlet anode and cathode, these values are used in modeling the Al/H_2O reactor and condenser. This is assuming the composition of the gases do not change between the exit of the Al/H_2O reactor and the SOFC anode inlet, and the cathode gases do not change between the exit of the condenser and the SOFC cathode inlet.

The Al/H_2O reactor takes the anode flow rates from the SOFC model and uses them with the relation between product and reactant species, Reaction 1.5, to solve for the inlet molar flow rate of H_2O, $\dot{n}_{H_2O,in,Al\_reac}$, and the amount of Al reactant.

$$2Al(s) + 3H_2O(l) \Leftrightarrow Al_2O_3(s) + 3H_2(g) \qquad \text{(Reaction 1.5)}$$

The amount of Al reactant stored in the reactor will depend on the conversion of H_2O to H_2. For this study it is assumed that 75% of H_2O is conversed to get 25 mol% H_2O out of the reactor (the maximum level of water desirable. Now masses of each reactant can be calculated for the specific energy and energy density calculations.

An energy balance is used to find the exhaust temperature of the Al/H_2O reactor as an input for the heat exchanger between the anode and cathode inlet

streams to the SOFC. The enthalpy values are calculated for the inlet, at T_{in,Al_reac} of 298.15K, and outlet, T_{out,Al_reac} being the value solved for in equation 4.8.

$$\sum h_{k,in}(T_{in,Al\_reac})\,\dot{n}_{k,in,Al\_reac} = \sum h_{k,out}(T_{out,Al\_reac})\,\dot{n}_{k,out,Al\_reac} + \dot{Q}_{loss,Al\_reac}$$

(eq. 4.8)

The $\dot{Q}_{loss,Al\_reac}$ assumes a *UA* value of 12 W/K in order to keep the temperature at the exit low enough to handle <1200 K.

For safety concerns, H_2O_2 must be stored in solution with H_2O at no more than approximately 60% by mass [47]. With a 60% by mass H_2O_2 solution, full conversion of H_2O_2 to H_2O and O_2 according to Reaction 1.6 under adiabatic conditions provides a two-phase output stream without fully vaporizing the flow.

$$H_2O_2(l) + xH_2O(l) \Leftrightarrow (1 + x)H_2O(g) + 0.5O_2(g) \qquad \text{(Reaction 1.6)}$$

With a value close to the vaporization temperature, it is ideal to condense out water from the flow. By doing so, more than 90% of the water from the H_2O_2 reactor outlet is condensed and circulated back to a water storage tank. This is calculated by setting the outlet temperature of the condenser to 335 K, leaving a mole fraction of 22% H_2O and 78% O_2 going out of the condenser. As seen from the SOFC button cell experiments, operating at low mol% H_2O and lower current densities will not likely affect cell performance at least for the length of durations tested in this study. The mole fraction of H_2O at the cathode inlet is specified through the condenser so as not to exceed experimental values.

The temperature between the H_2O_2/H_2O reactor exhaust and the condenser, approximately 373 K, is calculated through an energy balance between the product and reactant enthalpy values at the outlet temperature mentioned, and an inlet temperature of 340K, needed to get the reaction to occur. The H_2O_2 reactor model calculates the molar flow rates of H_2O_2 and H_2O reactants based on an approximation of 100% conversion of H_2O_2 to provide the necessary O_2 to the SOFC cathode. These molar flow rates are added to the total mass of the system for the energy density calculations.

The H_2O_2 decomposition reactor did not produce enough heat to directly feed the fuel cell cathode inlet with adequate inlet temperatures. For SOFCs within UUV designs it is ideal to operate at low O_2 stoichiometry so that oxidizer will be stored on board, improving the energy density. However, at low O_2 stoichiometry, the SOFC stack will heat up quicker, requiring a cooler inlet temperature of the reactants. The design of the SOFC heat release is very important and must be considered for a UUV application.

The temperature at the outlet of the condenser is specified for the maximum amount of H_2O desirable, close to the vaporization temperature. As discussed earlier in the section, the outlet flow from the condenser recovers excess heat in a heat exchanger with the hot H_2 flowing out of the Al/H_2O reactor. The heat exchanger model uses the outlet temperatures and molar flow rates from the Al/H_2O reactor and the condenser to calculate an inlet temperature to the fuel cell. From the heat exchanger model, the temperature can be adjusted by changing the *UA* value for the heat loss of the Al/H_2O reactor. The appropriate *UA* value of

12W/K is found to keep the SOFC inlet temperature within reasonable values (400-600 K).

The size and mass of the heat exchanger is calculated based on the area of heat transferred at an overall heat transfer coefficient of 80 W/m^2K. The area of heat transferred is calculated using the difference in enthalpy values of the inlet and outlet flows and the log mean temperature difference (lnMTD).

Table 4.2 lists the flow rate, temperature, and composition at each point in the system, specified in Figure 4.3, at the input values listed in Table 4.1. The cathode and anode exhaust flows react in a catalytic combustor downstream of the SOFC. The resultant water is condensed and recycled back into the water tank. The ability to recycle the water saves as much as 30 kg and 30 L of space, allowing the system to have an increase of specific energy by 25 Wh/kg, and energy density by 47 Wh/L for a 40 hour mission.

Table 4.2 Flow rate, temperature, and composition for points listed in Figure 4.1with SOFC operating conditions listed in Table 4.1.

Point	Flow Rate (mol/s)	Temp (K)	Composition (mol%)		
			H_2O	O_2	H_2
1	0.066	374	0.819	0.181	0.000
2	0.015	335	0.219	0.781	0.000
3	0.051	335	1.000	0.000	0.000
4	0.015	634	0.219	0.781	0.000
5	0.033	1184	0.250	0.000	0.750
6	0.033	634	0.250	0.000	0.750
7	0.005	923	0.628	0.372	0.000
8	0.033	923	0.850	0.000	0.150

4.1.1 Operating Parameters and Variables

The UUV power system is exposed to a range of operating conditions to assess how the system design might be impacted by desired range of operating conditions. The four main variables explored are operating voltage, U_{H2}, oxygen stoichiometry, and concentration of H_2O_2 in H_2O_2, listed in Table 4.3. SOFC operating temperature determines the effective ASR and OCV which can be used to specify current density over the SOFC stack for a given anode U_{H2} and cathode O_2 stoichiometry based on the SOFC button cell experiments. The operating voltage per cell (V/cell) is specified so as not to go below a potential that could degrade the cell under humidified fuel and oxidant streams. For button cell experiments, U_{H2} and U_{O2} is recommended to be $\leq$ 5% since there is not a defined flow field [48]. For SOFC stacks, higher U_{H2} (~80%) improves overall system energy densities. This parameter is varied to reflect the performance and to see its effect on the endurance of a UUV. The oxygen stoichiometric ratio is another parameter that will change how the SOFC operates and therefore altering the energy density of the system from the amount of oxygen consumed. It is also beneficial to explore the difference between the % H_2O_2 by mass in water since it is a major contributor to volume, mass, and respective energy density and specific energy.

Table 4.3 List of system variables explored to characterize the system.

Variable	Range
Operating Voltage (V)	0.8 – 0.7
Fuel Utilization (U_{H2})	0.7 - 0.9
Oxygen Stoichiometry	1.1 - 1.4
% H_2O_2 by mass in H_2O	0.6 – 0.7

4.2. UUV Energy Density and Mission Duration Study

The energy density specified for UUV mission requirements incorporates all of the power system components. For this study, the system includes fuel and oxidant reactors, heat exchangers, SOFC, fuel and oxidizer storage, and auxiliary components, electronics for gas flow control and sensors, piping, fans, pumps and tubing. The auxiliary was assumed to be about 6 kg and use up 6 L of space. These components also add to the parasitic loads, estimated to be 625 W (based on a balance of plant efficiency of 80%).

Table 4.4 Component list of mass and volume of constant value components and components changing with time at the SOFC conditions specified in Table 4.1.

Constant Value Component	**mass (kg)**	**volume (L)**
200 Cell Planar SOFC Stack	23.60	15.72
Heat Exchanger	0.89	0.4
Anode Water Reactant	0.65	0.65
Catalytic Combustor/HEX	1.25	0.75
Auxiliary	6	6
Component Changing with Time	**mass (kg/hr)**	**volume (L/hr)**
Aluminum Reactor	0.75	0.1
Aluminum Reactant	1.6	0.6
H_2O_2 Reactor, Condenser	0.18	0.13
H_2O_2 Reactant	2.95	2.18
Cathode Water Reactant	1.97	1.4
Neutral Buoyancy Adjust.	0	3.07
Total for 40 hour mission	**330.98 kg**	**322.95 L**

Weight and volume of system components are calculated to see what is significant to the density of the system. As displayed in Table 4.4, the largest

contributor to weight and volume of the system is the H_2O_2 reactant and its water for mission times in the range of 20 - 100 hours. To reduce this impact, the SOFC can be operated at a low O_2 stoichiometry or use a high content H_2O_2 (> 60% by mass), reducing the volume and mass of H_2O_2 and respective energy density and specific energy.

The water used in aluminum oxidation, however, does not have a large impact on the weight and volume due to the water recycle in the system. The flow rate of water exiting the fuel cell was greater than the flow rate going into the aluminum oxidation reactor. This would allow a water circulation loop to recycle the water in the system and store what is needed onboard. This reduces the weight and volume for the anode reactants, and a similar design is recommended for the H_2O_2 reactor for a future study. An overall reaction of what is occurring within the system can be seen in Reaction 4.1.

$$2Al + 3H_2O_2 \Leftrightarrow Al_2O_3 + 3H_2O \qquad \text{(Reaction 4.1)}$$

The products of the system are the solid aluminum oxide and H_2O. H_2O as a reactant allows the system to conveniently recycle water, reducing the overall energy density and specific energy.

60% H_2O_2 by mass in H_2O provides the O_2 through the decomposition reactor. At a higher mass fraction of H_2O_2, 70%, and at the same operating conditions, the amount of water required for the oxidizer decreases from 89 L to 57 L, thereby increasing the energy density by 65 Wh/L. Although, avoiding higher mass fractions of H_2O_2 will prevent any safety concerns of highly concentrated peroxide.

The variables listed in Table 4.4 are used to characterize the energy density of the system while operating under various parameters. While changing each parameter, all other inputs, seen in section 4.1, are kept constant. The voltage is defined for each cell for a 200 cell stack. For the baseline case with an estimated balance of plant efficiency η_{BOP} = 80%, the SOFC stack produces a total of 3.125 kWe with a net 2.5 kWe for the UUV propulsion and electrical loads. For the desired inlet operating voltage and power, the flow rates in and out of the SOFC were calculated as discussed previously. Current density, *i*, was initialized as the total power over the operating voltage. It should be noted that power electronics were not considered in this study as well as contributions of seawater heat exchangers.

The energy dependence on voltage over mission length in hours is shown in Figure 4.2. The minimum Navy requirement for specific energy and energy density for a HWV Class UUV are 300 Wh/kg and 360 Wh/L for a 40 hour mission time, respectively, and should be considered when assessing these specific energy and energy density charts. The specific energy and energy density calculations include neutral buoyancy so that the density of the UUV propulsion system falls within 1.05 – 1.01 kg/L. For the energy density curves, the voltage used to calculate the energy density and specific energy stayed consistent with the *V-i* curve given the *OCV* and *ASR* listed in Table 4.1.

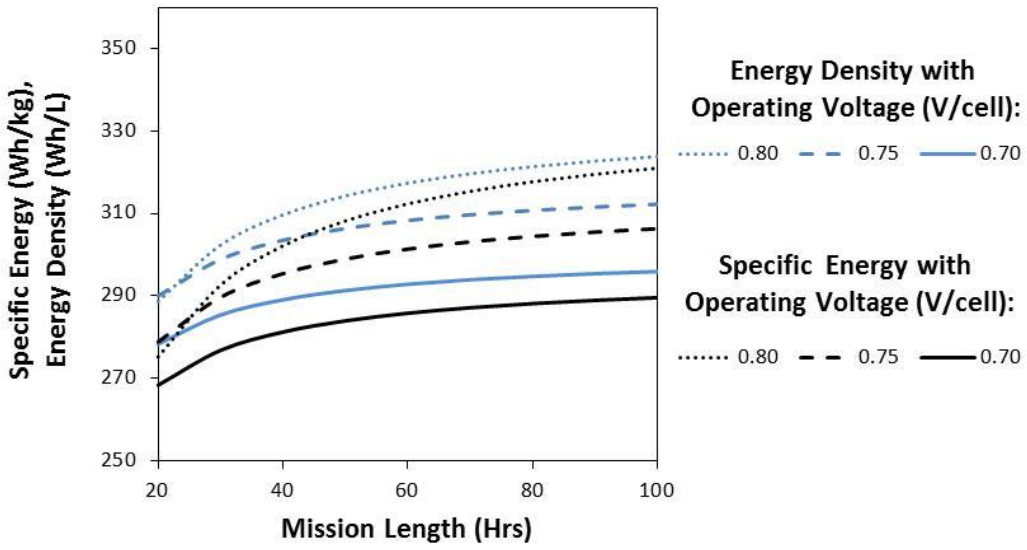

Figure 4.2 Specific energy and energy density dependence on operating voltage of the SOFC.

As seen in Figure 4.2, a higher operating voltage (0.8 V) increases the energy density by require a slower flow rate (less fuel/oxidizer needed). At short mission times close to 20 hours however, operating at 0.75 V increases the overall power density (W/cm^2) per cell, requiring half the size of a SOFC stack needed for operating at 0.8 V. This reduces the 200 cell stack size operating at 0.8 V to 90 cells operating at 0.75 V and 65 cells at 0.70 V operating voltage. Over time, total mass and volume become less dependent on the constant value components, in Table 4.4, and more dependent on the system components changing with time where the graph starts to level out.

As U_{H2} increases, more fuel is being consumed within the anode, therefore less fuel is needed for the SOFC. Figure 4.3 demonstrates this with specific energies increasing with U_{H2} and mission length.

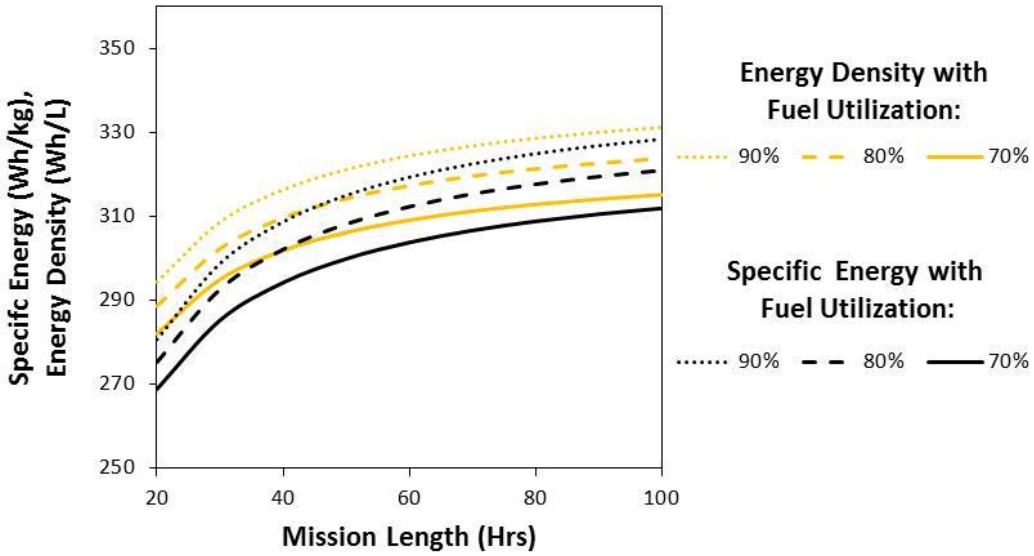

Figure 4.3 Graph of specific energy and energy density over mission length at three fuel utilization (U_{H2}) percentages.

Energy density has an even greater dependence on O_2 stoichiometry, as can be seen in Figure 4.4. The mass and volume of the oxidant, H_2O_2/H_2O mix contributes the most to the total out of all the SOFC power system components. Therefore, it is expected to see the energy density and specific energy primarily dependent on the O_2 stoichiometry. As more O_2 is consumed in the cathode, the less O_2 is wasted and the smaller amount of H_2O_2 is required on board.

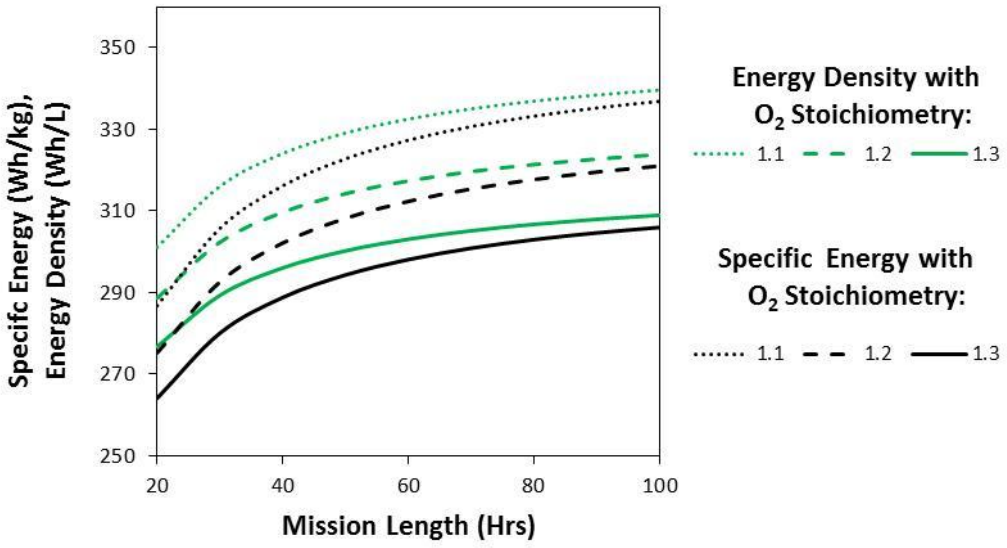

Figure 4.4 Graph showing the dependence of specific energy and energy density on O_2 stoichiometry.

In addition to the O_2 stoichiometry, another parameter that shows the energy density and specific energy dependence is H_2O_2 concentration in water. Figure 4.5 shows the % H_2O_2 and its contribution to the energy density and specific energy. At 70% H_2O, the energy density reaches 350 Wh/L at 100 hours although, as mentioned before, that high concentration is considered unsafe. Research into another type of oxidant that is not so dilute would be ideal for the maximum increase in energy density and specific energy. Restriction of high oxidant concentrations proves to be a significant drawback in attempts to improving energy densities of UUV propulsions systems.

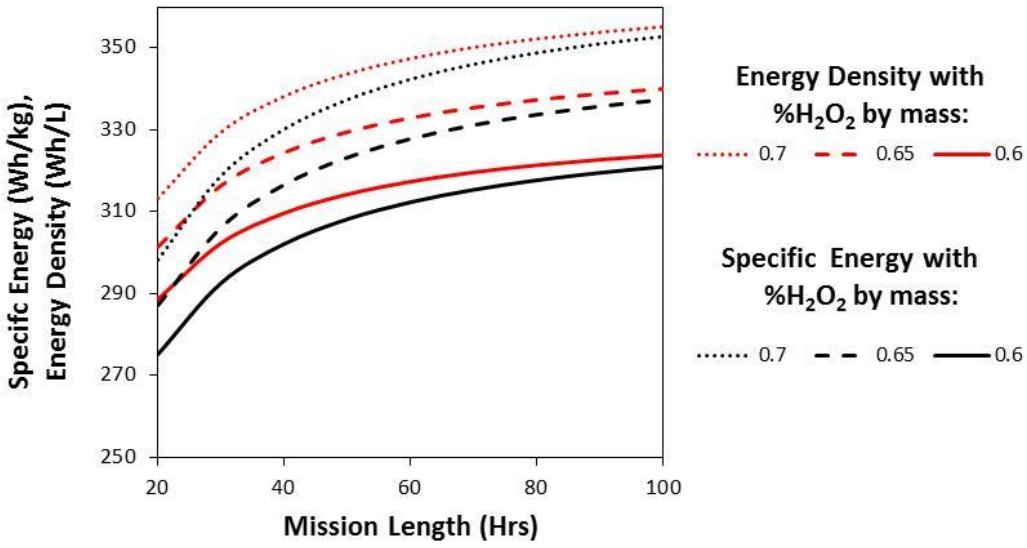

Figure 4.5 Graph showing the dependence of specific energy and energy density on % H_2O_2 by mass.

The four parameters reviewed, voltage, fuel utilization, O_2 stoichiometry, and % H_2O_2 by mass, showed the system's dependencies and provided a starting point for investigating the ideal operating conditions required for an energy dense SOFC system incorporated into a UUV. The system does not quite reach minimum requirements for energy density over a 100 hour UUV mission run time considering a neutrally buoyant system.

An interesting and valuable finding from this stack sizing exercise revealed that the heat removal from the system was significant, 14 kW. This value comes from a set heat loss *UA* value for the Al/H_2O reactor, set to 12 W/K, and the heat removed the SOFC stack to maintain stable temperatures with a heat loss *UA* value of 2.25 W/K. The 14 kW does not include the catalytic combustor heat

exchanger, also adding to the wasted heat. An attempt to make the system efficiently use the wasted heat was unsuccessful, providing an opportunity for further study and review of utilizing the heat in a more productive way to increase the energy density of the system.

Chapter 5: Conclusions and Future Work

Incorporating a LT SOFC into the power system design of a UUV was the prime focus of this paper. In this study, button cells were fabricated and tested to explore the feasibility of utilizing an air-independent, energy dense fuel (aluminum oxidation in water to make H_2) and oxidizer (decomposition of H_2O_2 to make O_2). Experimental results revealed the ideal operating conditions for a Ni/GDC/LSCF anode-supported SOFC while under humidified H_2 fuel at the anode and humidified O_2 oxidizer environment at the cathode. These results were used to scale up to a SOFC stack to estimate the size of a UUV power system, exploring the specific energy and energy density of the system over a typical UUV operating time of 20-40 hours.

5.1. Summary of Results

Ni/YSZ anode-supported button cells with Ni/GDC anode functional layers, GDC electrolyte layers, and composite LSCF/GDC cathodes were fabricated as described in Chapter 2, for experimental testing. Despite many efforts in making button cells, challenges arose in getting consistently high performance. One such difficulty was achieving a dense GDC electrolyte which helps to maximize the cell OCV, needed for MIEC doped ceria materials. This problem was mitigated by reducing the amount of binder additives, increasing the ball-milling time to 170 hours, adjusting the heating schedule, and controlling the

weight applied to the cell during sintering. After witnessing a dense electrolyte through SEM, the OCV doubled (increase by 0.4 V).

Experiments using these fabricated cells, reviewed in Chapter 3, involved setting up a testing station that could create an atmosphere to simulate an Al oxidation reactor exhaust for the anode gas line and a H_2O_2 decomposition reactor exhaust for the cathode inlet gas feed. Humidity tests determined that the performance of the button cells was acceptable at lower operating current densities. While operating at 650°C and exposed to 40 mol% H_2O at the anode, no significant degradation of voltage greater than 0.2 mV/hr was witnessed, running at 0.3 A/cm^2. Cathode humidity results showed greater degradation, more than 3.5 mV/hr after exposure to 50 mol% H_2O at 650°C at 0.3 A/cm^2. However, enhanced performance was seen while operating at 0.17 A/cm^2. Degradation at a higher current density was attributed to possible poisoning or restructuring of the cathode material. Enhanced performance had been witnessed in other studies and was credited to hydroxide ions formed on the electrolyte surface, generating O^{2-} ions available to conduct through the electrolyte.

Reactant depletion tests were also run with the fabricated SOFC button cells to simulate a decrease in fuel and oxidizer down the length of the channel in a typical SOFC stack manifold. For anode depletion tests, no changes were seen at the high voltage range down to 15 mol% H_2 ($P_{eff} = 6.5 \cdot 10^{-26}$). Cathode depletion tests showed an overwhelming shift in OCV between 0.05 and 0.21 bar P_{O2} due to the ceria in the GDC reducing, providing a greater affinity to conduct electrons across the electrolyte.

In Chapter 4, results from the SOFC button cell experiments are used in scaling up to a SOFC stack incorporated into a UUV power system design. The OCV, ASR are gathered from experiments, along with knowledge in humidity and depleted reactant gas environments, utilized in calculating/determining SOFC stack parameters. These parameters provide input for heat exchangers and fuel and oxidizer reactors upstream of the SOFC inlet. Each component is sized to determine the specific energy and energy density of the total system. By changing the operating voltage from 0.8 - 0.75 V, the U_{H2} from 70-90%, the O_2 stoichiometry from 1.3 – 1.1, and the concentration of H_2O_2 in water from 60 - 70%, the energy density increased due to the reduced amount of fuel/oxidant needed to sustain a UUV mission length between 20 and 100 hours. With H_2O_2 concentration at 70%, the resultant energy density was close to 350 Wh/L after 100 hours for a neutrally buoyant system. The system designed for this study did not reach minimal energy densities specified for a HWV Class UUV, although this study showed the principal restricting conditions for improving the energy density.

5.2. Recommended Future Work

The challenges faced in this study were at very different levels from fabrication methods to experimental testing and system design. The challenges with undetermined solutions provide an opportunity for future studies of incorporating LT SOFC into a UUV power system. A list of recommendations are included here:

1. Characterization of different cathode microstructures under humid conditions.
2. Further testing in humidity and fuel/oxidizer gas depletion.
    a. Longer stability tests >100 hours and at lower temperatures 500-600^{0}C.
    b. Use of O_2 rather than air for cathode experiments.
    c. Concurrent anode cathode flow conditions testing.
3. Research of fuel and oxidizer reactors and the ability to control exhaust composition.
4. Investigation of voltage degradation causes (silicate glassy phases, silicon poisoning).
5. SOFC power generation system analysis of efficient use or disposal of excess heat and changes that will affect energy density.

In fabricating SOFC button cells, cathode binder additive may be causing higher than desirable porosities that need to be addressed. A variety of cathode porosities should also be investigated to see if there are any changes in performance under humid conditions since LSM cathodes have been seen to restructure in the presence of humidity. Other ways to characterize the cathode could be through symmetric, electrolyte-supported cells, providing information on the overpotentials strictly associated with the cathode.

For SOFC button cell testing, longer stability tests >100 hours for humidity and depletion of H_2 and O_2 tests are needed to determine whether the

SOFC system could be used in a UUV for longer missions. Cathode humidity tests were run only at 650°C, so it is important to test at lower temperatures to see if it plays a role in voltage degradation.

Tests were run with air at the cathode whereas using O_2 with a diluent could allow better control of the inlet composition and also reflect a better simulation of the decomposition of H_2O_2. Testing also investigated the anode and cathode individually, although in the system, both the anode and cathode would experience humid atmospheres at the same time. Investigation of running concurrent humidified H_2 and O_2 flows is needed. It would also be beneficial to investigate different types of aluminum oxidation reactors and H_2O_2 reactors to see what technology could best control the exhaust composition. Further characterization of button cell EDS measurements at various cross-sections of the cathode would be ideal to investigate silicon poisoning after humidity tests.

The UUV power system design proposed in this study considered using heat from the aluminum oxidation reaction, although an abundance of heat needed to be removed from the system (14 kW) that could potentially be used in other ways. For future studies, exploration of a better UUV power system that would utilize the lost heat would be desired. The energy density of the system was highly dependent on the amount of H_2O and H_2O_2 needed to be stored on board the UUV. Re-organizing the system to efficiently recycle the water may increase system energy density.

The study of using a LT SOFC in a UUV power system has been initiated, but more work in this effort could prove this system to be a worthy design. A more in depth LT SOFC model would be ideal to further explore the potential for this system in hopes to predict changes in performance based off initialized operating conditions.

Bibliography

[1] A. A. Burke and L. G. Carreiro, "System modeling of an air-independent solid oxide fuel cell system for unmanned undersea vehicles," *Journal of Power Sources,* vol. 158, pp. 428-435, Jul 2006.

[2] "The Navy Unmanned Undersea Vehicle (UUV) Master Plan," ed: Department of the Navy, 2004.

[3] D. Waters and C. Cadou, "Modeling a hybrid Rankine-cycle/fuel-cell underwater propulsion system based on aluminum-water combustion," *Journal of Power Sources,* vol. 221, pp. 272-283, January 1, 2013 2013.

[4] T. G. Hughes. *The Impact of Power system Type and Vehicle Size of Range and Payload for UUVs*. Available: http://auvac.org/uploads/publication_pdf/Hughes%20UUST03.pdf

[5] A. Burke and L. Carreiro, "Solid Oxide Fuel Cells in Unmanned Undersea Vehicle Applications," ed, 2008.

[6] G. Griffiths, D. Reece, P. Blackmore, M. Lain, S. Mitchell, and J. Jamieson, *Proceedings of 14th Unmanned Untethered Submersible Technology*. Durham, 2005.

[7] O. Hasvold and N. Storkersen, "Electrochemical power sources for unmanned underwater vehicles used in deep sea survey operations," *Journal of Power Sources,* vol. 96, pp. 252-258, 2001.

[8] J. B. Lakeman, A. Rose, K. D. Pointon, D. J. Browning, K. V. Lovell, S. C. Waring, *et al.*, "The direct borohydride fuel cell for UUV propulsion power," *Journal of Power Sources,* vol. 162, pp. 765-772, 2006.

[9] Q. Cai, D. J. L. Brett, D. Browning, and N. P. Brandon, "A sizing-design methodology for hybrid fuel cell power systems and its application to an unmanned underwater vehicle," *Journal of Power Sources,* vol. 195, Oct 1 2010.

[10] A. A. Burke, L. G. Carreiro, and R. C. Urian, "Results Using Processed Acetylene Fuel Stream in Solid Oxide Fuel Cell Stack," *Journal of Fuel Cell Science and Technology,* vol. 7, p. 3, Jun 2010.

[11] A. A. Burke, L. G. Carreiro, and E. S. Greene, "Carbide-based fuel system for undersea vehicles," *Journal of Power Sources,* vol. 176, Jan 21 2008.

[12] L. G. Carreiro, A. A. Burke, and L. Dubois, "Co-generation of acetylene and hydrogen for a carbide-based fuel system," *Fuel Processing Technology,* vol. 91, Sep 2010.

[13] E. D. Wachsman and K. T. Lee, "Lowering the Temperature of Solid Oxide Fuel Cells," *Science,* vol. 334, Nov 18 2011.

[14] M. A. Laughton, "Fuel Cells," *Journal of Power Engineering,* pp. 37-47, 2002.

[15] M. Powell, K. Meinhardt, V. Sprenkle, L. Chick, and G. McVay, "Demonstration of a highly efficient solid oxide fuel cell power system using adiabatic steam reforming and anode gas recirculation," *Journal of Power Sources,* vol. 205, May 1 2012.

[16] S. B. Adler, "Factors governing oxygen reduction in solid oxide fuel cell cathodes," *Chemical Reviews,* vol. 104, Oct 2004.

[17] N. M. Sammes and Y. Du, "Fabrication and characterization of tubular solid oxide fuel cells," *International Journal of Applied Ceramic Technology,* vol. 4, 2007 2007.
[18] B. R. Sudireddy, P. Blennow, and K. A. Nielsen, "Microstructural and electrical characterization of Nb-doped SrTiO3-YSZ composites for solid oxide cell electrodes," *Solid State Ionics,* vol. 216, May 28 2012.
[19] K. L. Duncan, K. T. Lee, and E. D. Wachsman, "Dependence of open-circuit potential and power density on electrolyte thickness in solid oxide fuel cells with mixed conducting electrolytes," *Journal of Power Sources,* vol. 196, pp. 2445-2451, Mar 2011.
[20] J. Nielsen, A. Hagen, and Y. L. Liu, "Effect of cathode gas humidification on performance and durability of Solid Oxide Fuel Cells," *Solid State Ionics,* vol. 181, pp. 517-524, Apr 2010.
[21] S. H. Kim, K. B. Shim, C. S. Kim, J. T. Chou, T. Oshima, Y. Shiratori, *et al.*, "Degradation of Solid Oxide Fuel Cell Cathodes Accelerated at a High Water Vapor Concentration," *Journal of Fuel Cell Science and Technology,* vol. 7, p. 6, Apr 2010.
[22] B. Stoops, C. Nguyen, and M. Haberbusch, "Multifunctional Cryogenic Power System for Unmanned Underwater Vehicles," ed: AUVSI Unmanned Systems North America, 2009.
[23] W. E. Batton, K. D. Hotton, J. A. Peters, and M. Klanchar, "Oxygen Source for Underwater Vehicle Fuel Cells (Final Report)," ed: Office of Naval Research, 2002.
[24] P. Kim, D. J. L. Brett, and N. P. Brandon, "The effect of water content on the electrochemical impedance response and microstructure of Ni-CGO anodes for solid oxide fuel cells," *Journal of Power Sources,* vol. 189, Apr 15 2009.
[25] L. Holzer, B. Iwanschitz, T. Hocker, B. Muench, M. Prestat, D. Wiedenmann, *et al.*, "Microstructure degradation of cermet anodes for solid oxide fuel cells: Quantification of nickel grain growth in dry and in humid atmospheres," *Journal of Power Sources,* vol. 196, Feb 1 2011.
[26] L. Meda, G. Marra, L. Galfetti, F. Severini, and L. De Luca, "Nano-aluminum as energetic material for rocket propellants," *Material Science and Engineering,* vol. 27, pp. 1393-1396, 2007.
[27] (October 2012). *High Energy Density for UUV Applications*. Available: http://www.alumifuelpowertech.com/?page_id=271
[28] E. Lennon, A. A. Burke, M. Ocampo, and R. S. Besser, "Microscale packed bed reactor for controlled hydrogen peroxide decomposition as a fuel cell oxidant aboard unmanned undersea vehicles," *Journal of Power Sources,* vol. 195, pp. 299-306, Jan 2010.
[29] M. Wekesa and Y. Ni, "Mechanism of Hydrogen Peroxide Decomposition by Manganese Dioxide," *Tappi Journal,* vol. 2, pp. 23-26, 2003.
[30] A. Hagen, K. Neufeld, and Y. L. Liu, "Effect of Humidity in Air on Performance and Long-Term Durability of SOFCs," *Journal of the Electrochemical Society,* vol. 157, pp. B1343-B1348, 2010.

[31] H. Birol, T. Maeder, and P. Ryser, "Processing of graphite-based sacrificial layer for microfabrication of low temperature co-fired ceramics (LTCC)," *Sensors and Actuators a-Physical*, vol. 130, Aug 14 2006.
[32] F. Zhao and A. V. Virkar, "Dependence of polarization in anode-supported solid oxide fuel cells on various cell parameters," *Journal of Power Sources*, vol. 141, pp. 79-95, Feb 2005.
[33] M. Mori, T. Yamamoto, H. Itoh, H. Inaba, and H. Tagawa, "Thermal expansion of nickel-zirconia anodes in solid oxide fuel cells during fabrication and operation," *Journal of the Electrochemical Society*, vol. 145, Apr 1998.
[34] H. Hayashi, M. Kanoh, C. J. Quan, H. Inaba, S. R. Wang, M. Dokiya, *et al.*, "Thermal expansion of Gd-doped ceria and reduced ceria," *Solid State Ionics*, vol. 132, Jul 2000.
[35] V. M. Janardhanan, V. Heuveline, and O. Deutschmann, "Three-phase boundary length in solid-oxide fuel cells: A mathematical model," *Journal of Power Sources*, vol. 178, Mar 15 2008.
[36] J. J. Seo, J. Y. Kim, and K. Kim, "Thermal decomposition of PVB (polyvinyl butyral) binder in the MCFC (molten carbonate fuel cell)," *Bulletin of the Korean Chemical Society*, vol. 19, Apr 20 1998.
[37] G.-Z. Ke, H.-F. Xie, R.-P. Ruan, and W.-D. Yu, "Preparation and performance of porous phase changepolyethyleneglycol/polyurethane membrane," vol. 51, ed: Energy Conversion and Management, 2010.
[38] M. W. Barsoum, *Fundamentals of Ceramics*. Ipswich, MA: Institute of Physics Publishing, 2003.
[39] K. Maca, J. Cihlar, K. Castkova, O. Zmeskal, and H. Hadraba, "Sintering of gadolinia-doped ceria prepared by mechanochemical synthesis," *Journal of the European Ceramic Society*, vol. 27, pp. 4345-4348, 2007.
[40] F. Qiang, K. Sun, N. Zhang, X. Zhu, S. Le, and D. Zhou, "Characterization of electrical properties of GDC doped A-site deficient LSCF based composite cathode using impedance spectroscopy," *Journal of Power Sources*, vol. 168, Jun 1 2007.
[41] Y. J. Leng, S. H. Chan, and Q. L. Liu, "Development of LSCF-GDC composite cathodes for low-temperature solid oxide fuel cells with thin film GDC electrolyte," *International Journal of Hydrogen Energy*, vol. 33, pp. 3808-3817, Jul 2008.
[42] G. Chen, G. Guan, S. Abliz, Y. Kasai, and A. Abudula, "Rapid degradation mechanism of Ni-CGO anode in low concentrations of H(2) at a high current density," *International Journal of Hydrogen Energy*, vol. 36, Jul 2011.
[43] R. P. O'Hayre, *Fuel cell fundamentals*. Hoboken, NJ: John Wiley & Sons, 2006.
[44] N. Sakai, K. Yamaji, T. Horita, Y. P. Xiong, H. Kishimoto, M. E. Brito, *et al.*, "Effect of water on electrochemical oxygen reduction at the interface between fluorite-type oxide-ion conductors and various types of electrodes (vol 174, pg 103, 2004)," *Solid State Ionics*, vol. 176, pp. 2325-+, Sep 2005.

[45] J. Nielsen and M. Mogensen, "SOFC LSM:YSZ cathode degradation induced by moisture: An impedance spectroscopy study," *Solid State Ionics*, vol. 189, May 6 2011.

[46] E. Bucher, W. Sitte, F. Klauser, and E. Bertel, "Oxygen exchange kinetics of La0.58Sr0.4Co0.2Fe0.8O3 at 600 degrees C in dry and humid atmospheres," *Solid State Ionics*, vol. 191, Jun 2 2011.

[47] *Occupational Safety and Health Guideline for Hydrogen Peroxide*. Available: http://www.osha.gov/SLTC/healthguidelines/hydrogenperoxide/recognition.html#references

[48] (2007). *Introduction to Solid Oxide Fuel Cell Button Cell Testing*. Available: http://www.fchea.org/core/import/PDFs/Technical%20Resources/SOFCFG-ButtonCellTesting-07-015.pdf